



**HAL**  
open science

## Gas-liquid mass transfer around Taylor bubbles flowing in a long, in-plane, spiral-shaped milli-reactor

Mei Mei, Gilles Hébrard, Nicolas Dietrich, Karine Loubiere

### ► To cite this version:

Mei Mei, Gilles Hébrard, Nicolas Dietrich, Karine Loubiere. Gas-liquid mass transfer around Taylor bubbles flowing in a long, in-plane, spiral-shaped milli-reactor. *Chemical Engineering Science*, 2020, 222, pp.0. 10.1016/j.ces.2020.115717 . hal-02543386

**HAL Id: hal-02543386**

**<https://hal.insa-toulouse.fr/hal-02543386>**

Submitted on 16 Oct 2020

**HAL** is a multi-disciplinary open access archive for the deposit and dissemination of scientific research documents, whether they are published or not. The documents may come from teaching and research institutions in France or abroad, or from public or private research centers.

L'archive ouverte pluridisciplinaire **HAL**, est destinée au dépôt et à la diffusion de documents scientifiques de niveau recherche, publiés ou non, émanant des établissements d'enseignement et de recherche français ou étrangers, des laboratoires publics ou privés.



Open Archive Toulouse Archive Ouverte

OATAO is an open access repository that collects the work of Toulouse researchers and makes it freely available over the web where possible

This is an author's version published in: <http://oatao.univ-toulouse.fr/26779>

Official URL : <https://doi.org/10.1016/j.ces.2020.115717>

**To cite this version:**

Mei, Mei  and Hebrard, Gilles and Dietrich, Nicolas and Loubière, Karine   
*Gas-liquid mass transfer around Taylor bubbles flowing in a long, in-plane, spiral-shaped milli-reactor.* (2020) *Chemical Engineering Science*, 222. ISSN 0009-2509

Any correspondence concerning this service should be sent to the repository administrator: [tech-oatao@listes-diff.inp-toulouse.fr](mailto:tech-oatao@listes-diff.inp-toulouse.fr)

# Gas-liquid mass transfer around Taylor bubbles flowing in a long, in-plane, spiral-shaped milli-reactor

Mei Mei <sup>a,b,c</sup>, Gilles Hébrard <sup>a,c</sup>, Nicolas Dietrich <sup>a,c</sup>, Karine Loubière <sup>b,c,\*</sup>

<sup>a</sup> *Toulouse Biotechnology Institute, Université de Toulouse, CNRS, INRAE, INSA, Toulouse, France*

<sup>b</sup> *Laboratoire de Génie Chimique, Université de Toulouse, CNRS, INP, UPS, Toulouse, France*

<sup>c</sup> *Fédération de Recherche FERMAT, CNRS, Toulouse, France*



## A B S T R A C T

Gas-liquid mass transfer was investigated around Taylor bubbles flowing in a long, in-plane, spiral-shaped milli-reactor involving various configurations. Using a colorimetric technique and image post-treatment, the variation of the equivalent  $O_2$  concentration inside the liquid slugs was measured. The coloration positions, corresponding to 99% of the maximum concentration reached in the liquid slug, changed significantly under various operating conditions. Overall volumetric mass transfer coefficients were evaluated on the basis of these coloration positions, without considering the hydrodynamics change. The intensification factor of two configurations was found to be proportional to the increase in Dean number. Considering the changes in pressure drop, bubble length and velocity, the axial variation of cumulated mass flux could be measured. It decreased along tube and finally tended towards a constant value. A scaling law for the Sherwood number was proposed by introducing a normalized time, dimensionless liquid slug length, and the Péclet and Dean numbers.

## 1. Introduction

Gas-liquid mass transfer is a key phenomenon controlling the performances of multiphase reactors, which is widely encountered

\* Corresponding author at: Laboratoire de Génie Chimique, Université de Toulouse, CNRS, INP, UPS, Toulouse, France.

E-mail address: [Karine.loubiere@ensiacet.fr](mailto:Karine.loubiere@ensiacet.fr) (K. Loubière).

## Nomenclature

$A$	interfacial area in per unit cell, $m^{-1}$	$x$	horizontal axis in Cartesian coordinates, m
$C_{O_{2L}}^*$	oxygen concentration at saturation in the liquid phase, $kg\ m^{-3}$	$y$	vertical axis in Cartesian coordinates, m
$C_{O_{2L}}$	equivalent oxygen concentration in the liquid phase at a given location in the liquid phase, $kg\ m^{-3}$	<i>Greek symbols</i>	
$\bar{C}_{O_{2L}}$	average equivalent oxygen concentration in the liquid slug, $kg\ m^{-3}$	$\alpha_{O_2}$	mole fraction of $O_2$ in the gas phase, (-)
$C_{O_{2G}}$	oxygen concentration in the gas phase, $kg\ m^{-3}$	$\chi$	ratio of the amount of gas received from the LF to that received from the bubble caps, (-)
$D_{O_2}$	diffusion coefficient of $O_2$ , $m^2\ s^{-1}$	$\phi$	regression coefficient, $m^{-1}$
$d_{it}$	inner diameter of the spiral tube, m	$\Omega$	cross-sectional area of the tube, $m^2$
$d_B$	equivalent diameter with identical surface area of Taylor bubble, m	$\eta$	ratio of the superficial velocities of the gas and the liquid phases, (-)
$E$	chemical enhancement factor, (-)	$\mu_L$	dynamic viscosity of the liquid phase, Pa s
$F_1$	constant related to the variation of bubble length with $X$ , (-)	$\rho_L$	density of the liquid phase $kg\ m^{-3}$
$F_2$	constant related to the variation of bubble velocity with $X$ , $s^{-1}$	$\sigma_L$	surface tension of the liquid phase, $N\ m^{-1}$
$F_3$	constant related to the variation of bubble pressure with $X$ , $Pa\ m^{-1}$	$\lambda$	curvature ratio, (-)
$f$	frequency of circulation in the liquid slug, $s^{-1}$	$\omega$	linear dimensionless coefficient, (-)
$g$	gravitational acceleration, $m\ s^{-2}$	<i>Dimensionless numbers</i>	
$H$	Henry constant, $m^3\ Pa\ mol^{-1}$	$Ca$	$= \mu_L j_{TP} / \sigma_L$ Capillary number
$k_L$	liquid side mass transfer coefficient, $m\ s^{-1}$	$Sc$	$= \mu_L / \rho_L D_{O_2}$ Schmidt number
$k_L a$	overall volumetric mass transfer coefficient, $s^{-1}$	$De$	$= Re \times \sqrt{1/\lambda}$ Dean number
$j_G$	superficial velocity of the gas phase, $m\ s^{-1}$	$Re_{TP}$	$= \rho_L d_{it} j_{TP} / \mu_L$ two-phase Reynolds number
$j_L$	superficial velocity of the liquid phase, $m\ s^{-1}$	$Re_L$	$= \rho_L d_{it} j_L / \mu_L$ liquid Reynolds number
$j_{TP}$	total superficial velocity for two-phase flow, $m\ s^{-1}$	$Re_G$	$= \rho_G d_{it} j_G / \mu_L$ gas Reynolds number
$L_B(X)$	bubble length at a given axial position, m	$Pe$	$= ReSc$ Péclet number
$L_{BO}$	initial bubble length immediately after bubble formation, m	<i>Abbreviations</i>	
$L_S(X)$	liquid slug length at a given axial position, m	CFD	computational fluid dynamics
$\langle L_B \rangle$	average bubble length over the whole length of the tube, m	DH	dihydroresorufin
$\langle L_S \rangle$	average liquid slug length over the whole length of the tube, m	ET	external tubing
$M_{O_2}$	molar mass of $O_2$ , ( $kg\ mol^{-1}$ )	I.D.	inner diameter
$\varphi_{O_2}$	mass flux of $O_2$ transferred per unit of area, $kg\ m^{-2}\ s^{-1}$	LF	liquid film
$N$	number of the circulation loop, (-)	MT	medium tubing
$p_B$	pressure inside the bubble, Pa	RZ	resazurin
$p_{BO}$	initial pressure inside the bubble immediately after bubble formation, Pa	RF	resorufin
$Q$	volumetric flow rate, $m^3\ s^{-1}$	STD	standard deviation
$r$	radial coordinate of the spiral circle, m	$\langle \rangle$	mean value
$T$	temperature, K	<i>Subscripts and Superscripts</i>	
$t$	time, s	atm	atmospheric pressure
$t^*$	time normalized by coloration time, (-)	B	bubble
$U_{BO}$	initial bubble velocity immediately after bubble formation, $m\ s^{-1}$	BC	bubble caps
$U_B(X)$	bubble velocity at a given axial position, $m\ s^{-1}$	Exp	experimental data
$\langle U_B \rangle$	average bubble velocity over the whole length of the tube, $m\ s^{-1}$	G	gas phase
$V_B(X)$	volume of the bubble at a given axial position, $m^3$	$i$	integer number, (-)
$W$	dimensionless constant, (-)	$j$	integer number, (-)
$X$	axial position along the spiral tube from the bubble formation point, m	L	liquid phase
		Max	maximum
		Pre	predicted data
		R	real
		TP	two-phase flow
		UC	Unit Cell

in chemical engineering and environmental processes, such as organic photochemistry (Radjagobalou et al., 2018), hydrogenation reactions (Guo et al., 2019; Paul et al., 2018; Yue, 2017), oxidation reactions (Guo et al., 2017; Paul et al., 2018) or gas fermentation (Benizri et al., 2019; Garcia-Ochoa et al., 2010; Van Hecke et al., 2019). In particular, when the characteristic times of gas-liquid mass transfer are not short enough compared to those of the chemical reaction kinetics, low production yields and poor chemical

selectivity may be induced. Continuous-flow technologies, especially micro-structured reactors (i.e. microreactors, heat-exchanger reactors, monolith reactors, etc.), are now recognized as relevant alternatives for multiphase batch processing, and thus for process intensification (Gourdon et al., 2015; Jensen, 2001; Stankiewicz et al., 2019). Because of their small scale (diameters varying from a few tens of  $\mu m$  to less than 1 mm), they offer a high surface area to volume ratio and efficient mass and heat transfer

rates, thus providing higher yield and selectivity. The gas-liquid flow patterns at such a scale generally involve Taylor flows (Sobieszuk et al., 2012), as their segmented, regular structure leads to a further enhancement of gas-liquid mass transfer due to the circulation loops appearing in the liquid slug and to the liquid lubrication films at the walls.

Many questions remain to be addressed with respect to the strong coupling between local hydrodynamics, gas-liquid mass transfer and chemical reaction kinetics. For example, the size and velocity of a bubble may vary because of the mass transfer phenomenon and the pressure drop during the gas-liquid flow process in the microchannel (Eskin and Mostowfi, 2012; Nirmal et al., 2019; Zhang et al., 2018). For gases with high solubility, this is strongly pronounced, even more so when the transported gas is quickly consumed by a reaction in the liquid phase. Much research has been devoted to exploring these questions during the last decade, especially in the cases of confined configurations, such as Taylor flows. From an academic point of view, the latter confined configurations offer the advantage of enabling a detailed analysis of the local processes that is easier than can be obtained with bubble columns because the number of directions in which the bubbles can possibly move is reduced.

Most works consider Taylor bubbles flowing in a straight micro/milli channel or tube, as thoroughly reviewed by several authors (Abiev et al., 2017; Paul et al., 2018; Sattari-Najafabadi et al., 2018). On the other hand, curved channels or pipes have been found to give improved performances in terms of mixing (Fries and von Rohr, 2009; Kurt et al., 2017), and heat and mass transfer (Ghobadi and Muzychka, 2013; Kováts et al., 2018). However, investigations on gas-liquid hydrodynamics and mass transfer in curved channels are still rare, in particular for visualizing and measuring the transferred component concentration at local scale (Krieger et al., 2020; Krieger et al., 2017). Due to the bends or to the tube curvatures, a so-called Dean flow may be generated, characterized by the occurrence of secondary vortices (Fries and von Rohr, 2009). In the case of Taylor flows, the circulation loops in the liquid slug are no longer symmetrical about the centerline of the channel as in straight channels but present a complex three-dimensional structure in a bent channel (Krieger et al., 2019; Zalloha et al., 2012).

The overall mass transfer ( $k_L a$ ) in gas liquid Taylor flows in micro or milli devices has been intensively studied through different kinds of approaches, most of which are global methods although a few are local approaches. Numerous empirical and semi-empirical correlations have thus been put forward, as reported by Haase et al. (2016); Sattari-Najafabadi et al. (2018). These correlations (Bercic and Pintar, 1997; Van Baten and Krishna, 2004; Vandu et al., 2005; Yao et al., 2014, 2020; Yue et al., 2007) have pointed out the key factors that contribute to the mass transfer coefficients: the diffusion coefficient, unit cell length, bubble velocity, gas hold-up, liquid phase properties, etc. Nevertheless, these correlations, often dimensional, fail to capture the effect of the channel geometry and the physical mechanisms controlling mass transfer rates. Recently, Butler et al. (2018), Butler et al. (2016) and Abiev et al. (2019) applied the PLIF-I technique in a vertical millimetric channel (3 mm I.D.) to locally measure the oxygen concentration for Taylor flow. With specific image processing, they analyzed the separate contributions of the bubble caps and the lubrication films to the overall  $k_L a$ . They pointed out that the model proposed by Van Baten and Krishna (2004) was not able to predict the  $k_L a$  values for cases of slug length shorter than twice the channel diameter. These authors found that the overall  $k_L a$  was, in particular, proportional to the circulation frequency.

Some theoretical models (Sobieszuk et al., 2012; Svetlov and Abiev, 2016) have proposed interesting insights revealing the mass transfer mechanisms for Taylor flows, which include the gas trans-

ported: (1) from the bubble caps to the adjacent liquid slug, and (2) from the bubble body to the liquid film adjacent to the channel wall. These two parts are affected by the circulation motion in the liquid slug and by the saturation of the liquid film, respectively. As pointed by Nirmal et al. (2019), the main limitations of such models are that the bubble velocity and size are assumed constant throughout the channel and that the variation of the mass transfer coefficient during the dissolution process is not taken into account. Therefore, there is a need to identify the time or axial variation of the transport rates for process modelling purposes. A first attempt to describe and formulate the variation of mass transfer with time was presented by Pan et al. (2014) using experimental studies and CFD simulation. Later, the complete evolution of the spatial and temporal concentration field within the liquid slugs and the dynamic  $k_L a$  coefficients were presented by Yang et al. (2017b) who solved the coupled transport and reaction equations numerically. Other researchers (Yin et al., 2018; Zhang et al., 2018) have carried out experiments to measure these temporal evolutions of  $k_L$  (or variations of mass transfer with axial position in the channel). They also observed the decreasing trends of  $k_L a$  and  $k_L$  with increasing travel time in the channel (or axial position in the channel). Few studies (Eskin and Mostowfi, 2012) have studied the combined action of pressure drop and dissolution, although this case is commonly encountered in practice (the continuous-flow, micro-structured equipment involves long channels or tubes). The mechanism of this combined action of mass transfer and pressure drop under the continuous centrifugal force effect needs to be explored further.

Due to the shifted position of the circulation loops and the occurrence of secondary flow patterns, the gas-liquid mass transfer in curved channels is more complex than in straight channels. Recent studies have focused on hydrodynamics, heat transfer (Vashisth et al., 2008) and mixing (Zhang et al., 2016) for two-phase flow. Kurt et al. (2017) investigated the pressure drop and conversion of sodium sulfite in a coiled flow inverter (1 mm I.D.), finding a 14% higher conversion. Kuhn and Jensen (2012) compared the overall mass transfer coefficients in an in-plane spiral-shaped and a meandering channel using the pH-sensitive laser-induced fluorescence technique, and found a better mass transfer performance in the spiral-shaped device. (Kováts et al., 2018; Krieger et al., 2017, 2019, 2020; Yang et al., 2017a) have applied colorimetric techniques (i.e., using indigo carmine, methylene blue or resazurin) to visualize the oxygen concentration in helically coiled curved devices or meandering channels and observed the enhancement effects on mass transfer due to the centrifugal force.

In our preliminary study (Mei et al., 2020), the gas-liquid hydrodynamics (bubble velocity, bubble length and interfacial area, etc.) was characterized in a long, in-plane, spiral-shaped milli-reactor used for flow photochemistry applications (Aillet et al., 2016; Loubière et al., 2017). Two different configurations were considered, each presenting a different range of continuously changing curvature ratios. The variation of the hydrodynamic characteristics along the axial position in the tube was shown to be non-negligible, and their dependency on the gas-liquid two-phase superficial velocity, gas-liquid flow rate ratio and curvature ratio were clearly highlighted.

In keeping with this context, the present work reports investigations on the gas-liquid mass transfer process around Taylor bubbles flowing in the same long, in-plane, spiral-shaped milli-reactor as the one used in Mei et al. (2020). The resazurin-based colorimetric method described by Dietrich and Hebrard (2018); Dietrich et al. (2013, 2019), Kherbeche et al. (2019, 2013) and Liu et al. (2020) is implemented to measure the equivalent oxygen concentration fields inside the liquid slugs throughout the 3 m long tube. Two different configurations, in which the tube curvature changes continuously, are considered in order to cover a larger range of cur-

vature ratios (i.e., Dean numbers). The objective of these investigations is to better understand how gas-liquid mass transfer is affected by a continuous change of the channel curvature.

Section 2 describes the image post-treatment for mass transfer characteristics, in particular the specified calibration process. In Section 3, the results are presented in detail and discussed. The equivalent oxygen concentration fields in the liquid slugs are first reported at various operating conditions and a comparison is performed between the two configurations. Then, all the experimental data are brought together to propose a scaling law plotting the Sherwood number as a function of the normalized time and other dimensionless numbers.

## 2. Materials and methods

### 2.1. Experimental setup

The experimental setup was the same as the one used by Mei et al. (2020) and is shown in Fig. 1(a). The in-plane, spiral-shaped milli-reactor consisted of a Fluorinated Ethylene Propylene (FEP) tube (the inner and outer diameters were 1 mm and 3 mm), inserted inside a square channel carved into a flat Poly-Methyl-MethAcrylate (PMMA) plate and wound according to an Archimedean spiral geometry. Two configurations of tubing, named ET and MT (for External and Medium Tubing) were investigated: they had identical lengths (~3m) but differed by their wound positions on

the plate (see Fig. 1(b)). In this way, the intensity of the centrifugal forces could be changed while keeping the intensity of the inertial force constant.

The curvature ratio,  $\lambda$ , which varies with the radial position (i.e., the axial position) in the configuration, is defined as

$$\lambda = \frac{2r}{d_{it}} \quad (1)$$

where  $d_{it}$  is the inner diameter of the tube.  $r$  is the radial coordinate of the spiral circle under consideration (see Fig. 1(b)), which can be calculated from the equation describing the present Archimedean spiral shaped milli-reactor:

$$r = C_1 + C_2\theta, \quad (2)$$

where  $C_1$  is 5 mm and  $C_2$  is  $2/\pi$  mm rad<sup>-1</sup>,  $\theta$  (rad) being the angular coordinate. Mei et al. (2020) showed how to convert the spiral radius  $r$  into the axial position  $X$ . At last, the curvature ratio ranged from  $\lambda_{\min} = 124$  to  $\lambda_{\max} = 166$  for the ET configuration and from  $\lambda_{\min} = 52$  to  $\lambda_{\max} = 116$  for the MT configuration. The associated averaged curvature ratios,  $\langle \lambda \rangle$ , calculated as  $\langle \lambda \rangle = (\lambda_{\max} + \lambda_{\min})/2$ , for ET and MT were 145 and 84, respectively. The average Dean number,  $\langle De \rangle$ , can be calculated as:

$$\langle De \rangle = Re \sqrt{\frac{1}{\langle \lambda \rangle}} \quad (3)$$

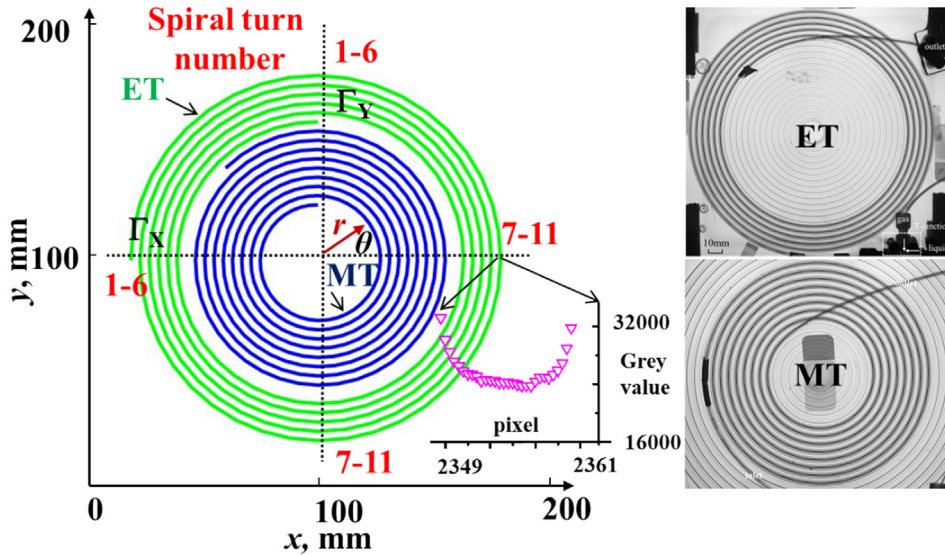
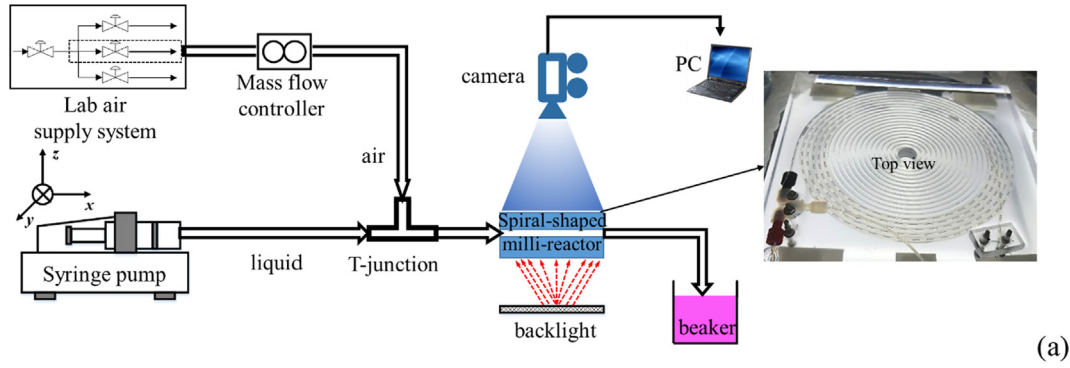


Fig. 1. (a) Schematic diagram of the experimental setup; (b) Schematic representation of the spiral-shaped milli-reactor viewed from the top, showing the tubing configuration (ET: External Tubing; MT: Medium Tubing) and radial profile of the pixel gray value along one tube cross-sectional direction.  $\Gamma_x$  and  $\Gamma_y$  are two orthogonal lines.

The Reynolds number,  $Re$ , is defined by the two-phase superficial velocity  $j_{TP}$ :

$$Re_{TP} = \frac{\rho_L d_{it} j_{TP}}{\mu_L} \quad (4)$$

where  $\rho_L$  and  $\mu_L$  are the density and dynamic viscosity of the liquid, respectively.

The values of  $\langle De \rangle$  and  $Re_{TP}$  are reported for each operating condition in Tables S1 and S2 of the Supplementary Material, as well as averaged bubble length  $\langle L_B \rangle$ , liquid slug length  $\langle L_S \rangle$ , bubble velocity  $\langle U_B \rangle$ , initial bubble length  $L_{B0}$  and its increasing rate  $F_1$ , initial bubble velocity  $U_{B0}$  and its increasing rate  $F_2$ , and initial pressure inside bubble  $p_{B0}$  and its decreasing rate  $F_3$ , calculated according to Mei et al. (2020). These parameters will be later used to calculate the average overall volumetric mass transfer coefficient and axial evolution of the mass flux density and Sherwood number in Sections 3.3–3.5.

Air was used as the gas phase and the flow rates were controlled by a HORIBA STEC airflow controller (Model: SEC-Z512MGX or SEC-7320, Accuracy:  $\pm 0.25\%$ ). The liquid phase consisted of solutions containing D-glucose anhydrous (Fischer-Scientific, CAS 50-99-7) at a concentration of  $20 \text{ g L}^{-1}$ , sodium hydroxide (VWR, CAS1310-73-2) at a concentration of  $20 \text{ g L}^{-1}$ , and resazurin (Sigma Aldrich, CAS 62758-13-8, molar mass  $229.19 \text{ g mol}^{-1}$ , purity 84%, noted RZ) at a concentration of  $0.105 \text{ g L}^{-1}$  (corresponding to  $0.125 \text{ g L}^{-1}$  of weighed RZ). The liquid was pumped by a neMESYS syringe pump (Model: NEM-B100-01 A) equipped with a 100 mL Harvard Instruments syringe and the liquid flow rates were regulated by a mass flow control system (Model: NEM-B100-01 A).

The in-plane, spiral-shaped milli-reactor was lit by a Phlox-LedW-BL LED backlight ( $300 \times 220 \text{ mm}$ ) and the images of the bubbles flowing along the tube were recorded by a 16-bit sCMOS PCO Edge camera. The image resolution was  $2560 \times 2160 \text{ px}^2$ . The camera was equipped with a Nikon AF micro Nikkor f/2.8 lens. During the experiments, the entire milli-reactor was placed in a glass tank filled with water to minimize optical distortion (the refractive index of FEP material being 1.34 (Hosoda et al., 2014) almost equals to the 1.33 of water).

## 2.2. Gas-liquid mass transfer image processing

The colorimetric technique proposed by Dietrich et al. (2013) is based on an oxygen-sensitive dye, resazurin (RZ), which can react with oxygen in the presence of sodium hydroxide (NaOH) and glucose solution. In the reduced form, named dihydroresorufin (noted DH), the solution is colorless while, in presence of oxygen, the oxidized form, named resorufin (noted RF), is characterized by an intense pink color. As shown in previous works, the main advantage of this technique is that the extent of the oxidation reaction which corresponds to the amount of oxygen transferred (or dissolved) accounting for the stoichiometric coefficient, is directly proportional to the color intensity (gray value) for a given concentration of resazurin.

After the image acquisition, the gas-liquid mass transfer characteristics were determined by three main image processing steps (implemented in MATLAB R2017b<sup>®</sup>): (i) extraction of liquid slugs and bubbles from the images; (ii) determination of the calibration curve; and (iii) conversion, pixel-by-pixel, of the gray values in the liquid slugs into equivalent oxygen concentrations. The term “equivalent” is used because, in reality, the oxygen concentration in the liquid phase was zero: oxygen was fully consumed by DH as long as there was enough DH in the liquid (see Yang et al., 2016).

For the calibration process, five groups of resazurin solutions at different concentrations (purity being considered) were prepared:

0.021, 0.042, 0.0763, 0.084 and  $0.105 \text{ g L}^{-1}$ . At each given RZ concentration, 200 frames containing fully saturated solution (i.e., pink RF) were taken. This process was repeated three times with solutions of the same concentration to reduce experimental uncertainties. Finally, for each RZ concentration, a time-averaged gray value image was obtained by averaging the 200 images to eliminate the slight deviation between instantaneous gray values.

To enable the variation of the concentration to be followed along the tube length, global images of the entire spiral-shaped milli-reactor were taken, thus leading to wide observing windows (ET:  $197.99 \times 167.05 \text{ mm}^2$ , MT:  $138.53 \times 116.75 \text{ mm}^2$ ). Due to these wide observing windows, and also to the circular cross section of the FEP tube, we noticed significant deviations in gray values for the same RZ concentration, depending on the spiral turn and on the radial positions at a given spiral turn.

Fig. 1(b) shows (in insert) that, for the  $0.042 \text{ g L}^{-1}$  of RZ, the gray values were not uniform along the  $\Gamma_x$  direction of spiral turn 11: they were lower at the centerline of the tube and higher at the edge of the tube wall (note that gray value ranged from 0 to  $2^{16}-1$ , corresponding to black and white respectively). This parabolic shape of the gray value distribution was due to the variable liquid thicknesses along the tube circular cross section, which led to more dark color (i.e. smaller gray values) being cumulated at the centerline of the tube. To overcome this issue of non-uniform distribution, a pixel-by-pixel calibration was applied to minimize the errors, which meant that the calibration relation curve was calculated independently, pixel by pixel. Fig. 2(a) shows typical relationships between the equivalent  $O_2$  concentration and the normalized difference of gray value,  $\Delta G$ :

$$\Delta G = \frac{I_0 - I}{I_{00}} \quad (5)$$

where  $I_0$  and  $I$  are the gray intensities at a zero resorufin concentration and at a given concentration, respectively, and  $I_{00}$  is the maximum 16-bit intensity, at  $2^{16}-1$ .

In Fig. 2(a), two representative pixels, named Pixel 1 and Pixel 2, have been chosen from the images to show the regressed linear relations using the least squares method (the standard deviation varied between 10% and 17%). Pixels 1 and 2 represented the pixels with 10% and 17% standard deviation, and were close to the tube wall and the tube centerline, respectively. Because of the changing thickness at different radial positions, more intensities cumulated around the tube centerline, leading to larger values of  $\Delta G$  for the Pixel 2. After applying the pixel-by-pixel calibration (more details of the benefits were reported in the Supplementary Material) to the raw image (Fig. 2(b)), the corresponding equivalent  $O_2$  concentration field was obtained, as illustrated in Fig. 2(c). All parts except for those corresponding to the liquid slugs were erased and set to zero concentration, i.e., blue color in Fig. 2(c).

## 3. Results and discussion

By implementing the colorimetric technique and developing ad hoc image processing to consider the Archimedean spiral shape of the tubing, the axial evolution of equivalent  $O_2$  concentration fields in the liquid slugs and the transferred  $O_2$  mass flux can be obtained and further used to deduce a scaling law.

### 3.1. Equivalent oxygen concentration fields

After applying the pixel-by-pixel calibration, the equivalent  $O_2$  concentration in the liquid slug of one Unit Cell (averaged over the tube depth), was extracted at a certain axial position  $X$  (the mass centroid position of the liquid slug) from the image processing as follows:

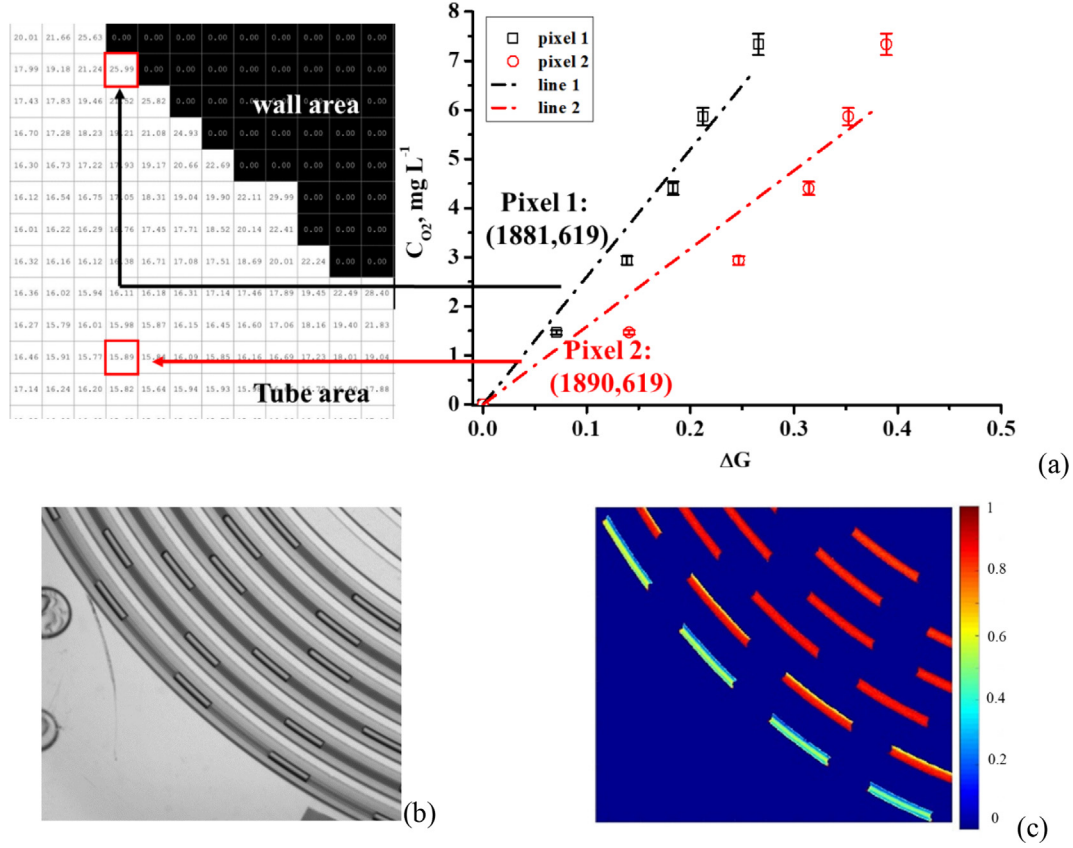


**Fig. 2.** (a) Examples of individual linear calibration curves between gray value differences and equivalent  $O_2$  concentration for two representative pixels on the image; (b) Partial raw image of gas-liquid flows; (c) Partial equivalent  $O_2$  concentration field (normalized by the maximum concentration). Operating conditions:  $Re_G = 0.9$ ,  $Re_L = 16.2$ ,  $Re_{TP} = 24$ ,  $\eta = 0.45$ ,  $\langle De \rangle = 2.0$ , ET.

$$\overline{C_{O_{2L}}(X)} = \frac{\iiint C_{O_{2L}}(x, y) dx dy dz}{\langle L_s \rangle \Omega} \quad (6)$$

where  $\Omega$  is the cross-sectional area of the tube and  $X$  represents the distance from the T-junction, i.e.,  $X = 0$  is the position of bubble formation. It is important to note that this integral was calculated by considering only the liquid slug volume, and not the liquid film around bubbles. Unfortunately, due to the limited resolution of the camera and to the tiny thickness of the liquid film assuming the latter would occur (noted  $\delta$ , varying from 3 to 16  $\mu m$  according to Mei et al. (2020)), the concentration in the liquid film could not be measured.

Fig. 3(a) presents the equivalent  $O_2$  concentration fields in the liquid slugs along the axial positions in the tube for the ET configuration. The time indicated in the figure corresponds to the time required for the liquid slug, in the black box, to travel to that position from the T-junction (where gas and liquid started to contact), and the liquid slug in the black box represents the liquid slug considered. It can be observed that, as the bubbles flowed along the channel, the amount of equivalent  $O_2$  in the liquid slug increased gradually until an equilibrium steady state was reached (no more color change, i.e., no more RF increase).

From the flow patterns inside the liquid slug visualized in Fig. 3 (b) and (c), the symmetrical liquid circulation loops that appeared inside the liquid slugs for straight tubes could no longer be observed when the  $\langle De \rangle$  increased. In Fig. 3(d), with a further increase of  $Re_{TP}$  and  $\langle De \rangle$ , the reactive RF color had a more uniform distribution in the liquid slug compared to the previous two cases. The equivalent  $O_2$  concentration fields were thus affected by the centrifugal force: the half loop of Taylor recirculation near the outer wall (observed close to the T-junction) was progressively

squeezed and quickly renewed to reach at higher and almost uniform concentration, as recently observed by Krieger et al. (2019).

Fig. 4 shows the variation of the average equivalent  $O_2$  concentration inside the liquid slug, normalized by the maximum concentration  $C_{max}$  in the liquid slug, along the axial position, for both tubing configurations (i.e., ET and MT), and with two identical sets of operating conditions (with same  $Re_{TP}$  and gas-liquid flow rate ratio  $\eta = j_G/j_L$ ). Firstly, a good fit with experimental data was obtained using the function  $\frac{C_{O_2}}{C_{max}} = 1 - \exp(-\phi X)$ , where  $\phi$  is a regression coefficient dependent on the operating conditions. Relative errors between fitted and experimental data were smaller than 5% for all the operating conditions. Secondly, whatever the operating conditions, the equivalent  $O_2$  concentration increased rapidly along the tube until it reached a constant value, i.e.,  $\frac{C_{O_2}}{C_{max}} = 1$ . When all the molecules of DH were consumed by the transferred oxygen or a quasi-steady state was achieved (no more effective mixing), there was no more change in the equivalent  $O_2$  concentration. For the RZ concentration used (0.105  $g L^{-1}$ ), this occurred for axial locations  $X$  larger than 1 m, whatever the operating conditions (Fig. 4).

To uncouple the effects of centrifugal forces from the inertial forces, it was necessary to fix the  $Re_{TP}$ , the average Dean numbers in MT being 1.31 times higher than in ET ( $\langle De \rangle_{MT} = 1.31 \langle De \rangle_{ET}$ ). In Fig. 4, at identical  $Re_{TP}$  and  $\eta$  (ratio of the superficial velocities of the gas  $j_G$  and the liquid phases  $j_L$ ) and for the same axial position  $X$ , the equivalent  $O_2$  concentration was significantly higher in the MT than that in the ET. This indicated that there was a significant intensification of mass transfer rates caused only by the centrifugal force (i.e. by reduced tube spiral radius), leading to a faster increase of the equivalent  $O_2$  concentration in the MT configuration.

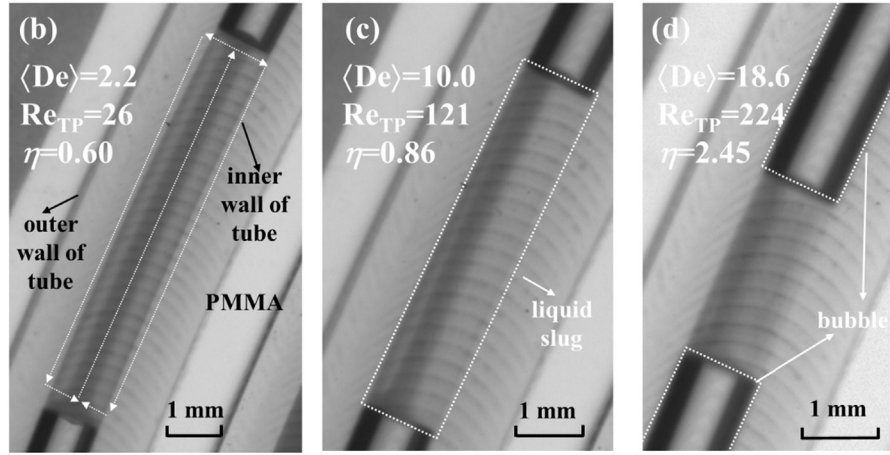
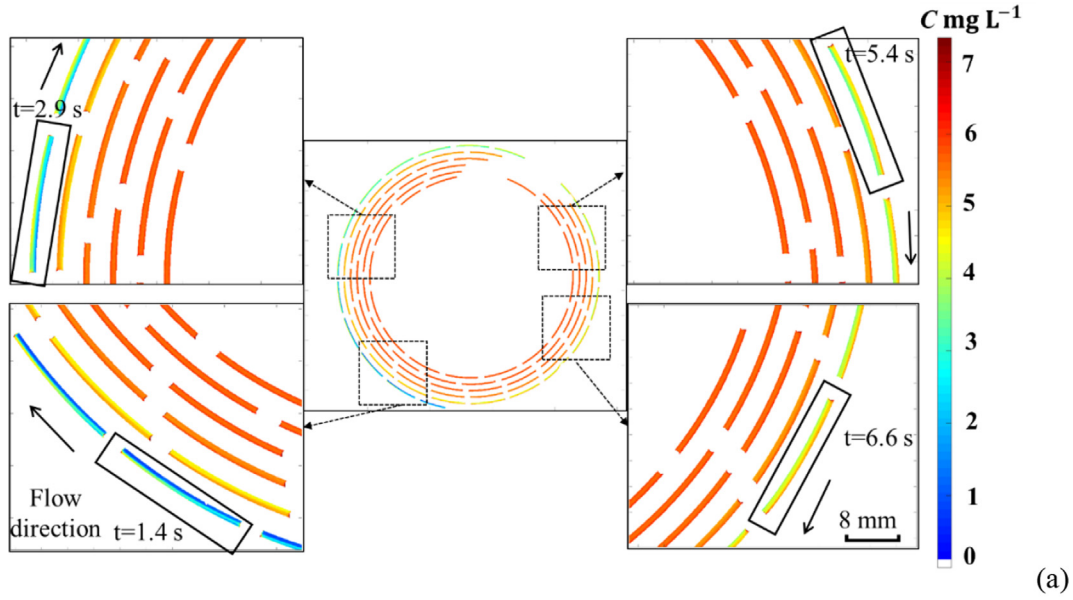


**Fig. 3.** (a) Equivalent  $O_2$  concentration fields in the liquid slugs: the time indicated in the figure corresponds to the time required for the liquid slug (in the black box), to travel to that position from the T-junction and the liquid slug in the black box represents the liquid slug considered (operating conditions:  $Re_L = 64.9$ ,  $Re_G = 1.5$ ,  $Re_{TP} = 78$ ,  $\eta = 0.2$ , and  $\langle De \rangle = 6.5$ , ET, flow direction is indicated using arrows). (b), (c), (d) Local raw visualization of the reactive RF color distribution in the liquid slugs at  $X = 0.1$  m, operating conditions: (b)  $Re_L = 16.2$ ,  $Re_G = 1.2$ ,  $Re_{TP} = 26$ ,  $\eta = 0.6$  and  $\langle De \rangle = 2.2$ ; (c)  $Re_L = 64.9$ ,  $Re_G = 6.7$ ,  $Re_{TP} = 121$ ,  $\eta = 0.86$  and  $\langle De \rangle = 10.0$ ; (d)  $Re_L = 64.9$ ,  $Re_G = 19.1$ ,  $Re_{TP} = 224$ ,  $\eta = 2.45$  and  $\langle De \rangle = 18.6$ ; ET). (For interpretation of the references to color in this figure legend, the reader is referred to the web version of this article).

The axial positions at which 99% of  $C_{max}$  was achieved, noted  $X_{coloration}$ , are plotted in Fig. 5 for all the operating conditions. Generally,  $X_{coloration}$  was achieved after a second spiral turn for ET and MT. It can be seen that  $X_{coloration}$  values were smaller in the MT configuration than in the ET, thus confirming that the centrifugal force had an intensification effect on the mass transfer rates. In addition,  $X_{coloration}$  decreased with increasing  $\eta$  (i.e., gas Reynolds number  $Re_G$ ) at a given liquid Reynolds number  $Re_L$ , which corresponded to a faster achievement of  $C_{max}$  in shorter liquid slugs and higher  $Re_{TP}$ .

When  $Re_L$  was much higher than  $Re_G$ , (small  $\eta$ , see the solid blue triangle point in Fig. 5, the ratio between the average liquid slug length and bubble length,  $\langle L_S \rangle / \langle L_B \rangle$ , was 3.5 (meaning very long liquid slugs), and the distances required to reach  $C_{max}$  were significantly longer than under other conditions.

### 3.2. Average overall volumetric mass transfer coefficient

As the experiments were carried out in long tubes ( $\sim 3$ m), Mei et al. (2020) observed non negligible changes of the bubble length

(noted  $L_B$ ) and bubble velocity (noted  $U_B$ ) along the length of the tube, and a significant pressure drop. Two different mechanisms may have contributed to such variations: pressure drop and mass transfer of  $O_2$  from the gas to the liquid, and they have opposite effects: mass transfer of  $O_2$  from gas to liquid tends to decrease the bubble volume while the pressure drop results in gas expansion. The centrifugal effects induced by the tube curvature (Dean number) may also act on these phenomena and modify their contributions. For these reasons, in the following calculations, the variation of bubble volume and velocity, and the pressure drop along the tube should be considered.

The overall volumetric mass transfer coefficient  $k_L \cdot a$  along the tube length can be deduced from the oxygen mass balance in the liquid phase, and may change during the mass transfer process (instead of assuming a constant value):

$$\frac{d\overline{C_{O_{2L}}(X)}}{dt} = E k_L(X) a(X) (C_{O_{2L}}^*(X) - \overline{C_{O_{2L}}(X)})_r \quad (7)$$

where  $t$  represents the traveling time corresponding to  $X$  ( $t = X / U_B$ ) and  $\overline{C_{O_{2L}}(X)}_r$  is equal to zero because of a fully consumption of  $O_2$  by

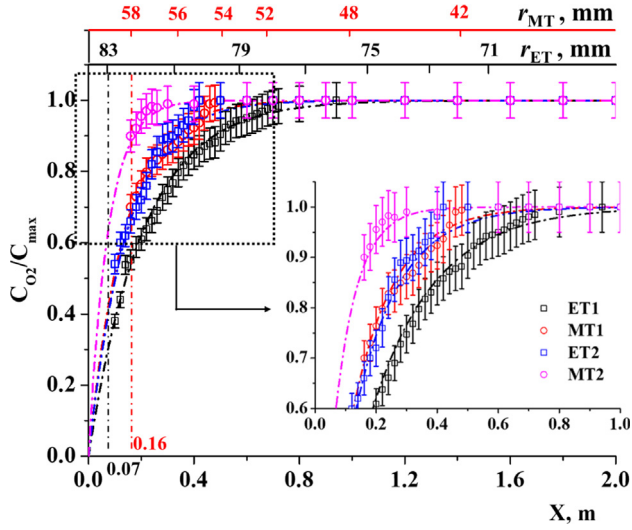


**Fig. 4.** Comparison of the axial evolution of normalized average equivalent  $O_2$  concentration in the liquid slug along the channel for different operating conditions (ET1 and MT1:  $Re_L = 16.2$ ,  $Re_G = 1.2$ ,  $Re_{TP} = 26$ ,  $\eta = 0.60$ ; ET2 and MT2:  $Re_L = 32.4$ ,  $Re_G = 10.0$ ,  $Re_{TP} = 116$ ,  $\eta = 2.58$ ). Here the points and lines represent experimental and calculated data, respectively. The second abscissa axis (at the top) gives the spiral radius for each configuration, corresponding to the axial position (reported on the principal abscissa axis, at the bottom).

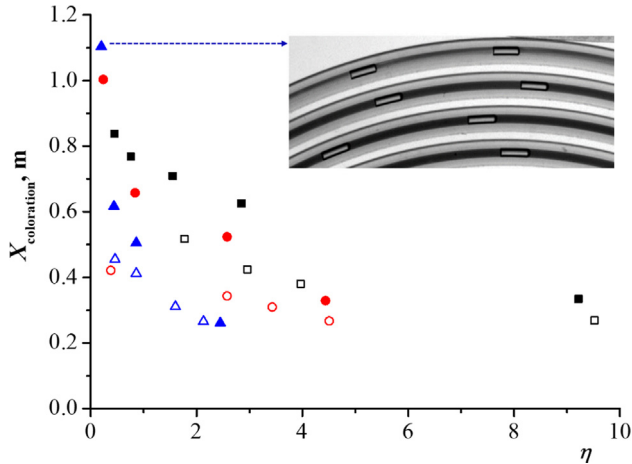


**Fig. 5.** Variation of the axial position  $X_{\text{coloration}}$  for which  $C_{\text{max}}$  is achieved with the gas-liquid superficial velocities ratio  $\eta$ , solid and empty symbols represent ET and MT,  $Re_L$  of black, red and blue color: 16.2, 32.4 and 64.9. (For interpretation of the references to color in this figure legend, the reader is referred to the web version of this article).

DH in the liquid slug.  $E$  is the chemical enhancement factor, which is the ratio between the average mass fluxes with the resazurin-based reaction, and with the pure physical absorption, and  $C_{O_{2L}}^*$  is the  $O_2$  concentration at saturation (calculated accounting for pressure drop, see Supplementary Material). Note that all the parameters involved in Eq. (7) depend on the axial position.

To calculate the overall volumetric mass transfer coefficient,  $k_L \cdot a$ , simply and directly, it was assumed in a first step that  $C_{O_{2L}}^*$  and  $k_L \cdot a$  were kept constant during the whole mass transfer process and using the average gas-liquid hydrodynamics, e.g.,  $\langle U_B \rangle$ . From the stoichiometry of dihydroresorufin and  $O_2$ , two moles of DH react with one mole of  $O_2$ , and the relationships between  $\overline{C_{O_{2L}}(X)}$  and the resazurin concentration are (Dietrich et al., 2019):

$$\frac{1}{M_{O_2}} \frac{d\overline{C_{O_{2L}}}}{dt} = -\frac{1}{2} \frac{dn_{DH}}{dt} = -\frac{1}{2} \frac{1}{M_{RZ}} \frac{dC_{RZ}}{dt} \quad (8)$$

where  $M_{O_2}$  and  $M_{RZ}$  are the molar masses of  $O_2$  and resazurin, respectively.  $n_{DH}$  and  $C_{RZ}$  are the molar amount of DH and the mass concentration of resazurin, respectively.

In addition, the volumetric overall  $k_L \cdot a$  can be deduced from Eq. (7). Various authors (Dietrich et al., 2019; Yang et al., 2017a) have found that the enhancement factor  $E$  is equal to 1 when the order of magnitude of  $k_L$  was about  $10^{-4} \text{ m s}^{-1}$ , typically in milli-reactors. Therefore,  $E$  was considered equal to 1 here.

By combining Eq. (7) and Eq. (8) and integrating from  $t = 0$  to the full coloration time,  $t_{\text{coloration}}$ , the following equation can be thus deduced to obtain the average overall volumetric mass transfer coefficients, noted  $\langle k_L \cdot a \rangle$ :

$$\langle k_L \cdot a \rangle = \frac{C_{RZ}}{\langle C_{O_{2L}}^* \rangle} \cdot \frac{M_{O_2}}{2M_{RZ}} \cdot \frac{1}{t_{\text{coloration}}} \quad (9)$$

where the saturation time  $t_{\text{coloration}}$  equals  $X_{\text{coloration}}/\langle U_B \rangle$ .

Similarly, the Eq. (9), in which  $C_{RZ}$  is included, is a general formula to easily link  $t_{\text{coloration}}$  and  $\langle k_L \cdot a \rangle$ , as adopted in Dietrich et al. (2019) for bubbles rising in stagnant liquid. As long as the axial location ( $X_{\text{coloration}}$ ) where the full coloration is achieved is deduced for each operating condition (shown in Fig. 5),  $\langle k_L \cdot a \rangle$  can be directly evaluated from Eq. (9).

As the mass transfer mechanism was affected by the Taylor vortices inside the liquid slug, it was interesting to consider the frequency of loop circulations adopted from (Abiev et al., 2019) as:

$$f_c = \frac{j_{TP} - \langle U_B \rangle / 2}{2(L_S)} \approx \frac{\langle U_B \rangle}{4(L_S)} \quad (10)$$

which reflects the amount of elementary mass transfer per unit of time.

In Fig. 6, the average overall volumetric mass transfer coefficient,  $\langle k_L \cdot a \rangle$ , (deduced from Eq. (9)) is plotted against the frequency of circulations  $f_c$ . It can be seen that (i) whatever the tubing configuration,  $\langle k_L \cdot a \rangle$  varied linearly with  $f_c$ , which is physically consistent, and (ii) at the same  $f_c$ ,  $\langle k_L \cdot a \rangle$  were rather higher in MT than in ET.

To better quantify the latter observation, these average overall coefficients were fitted by linear relations using least squares regression, as follows,

$$\langle k_L \cdot a \rangle = \omega f_c \quad (11)$$

where  $\omega$  is a linear dimensionless coefficient that depends on the tubing configurations.

The intensification factor of centrifugal force for two configurations was introduced as:

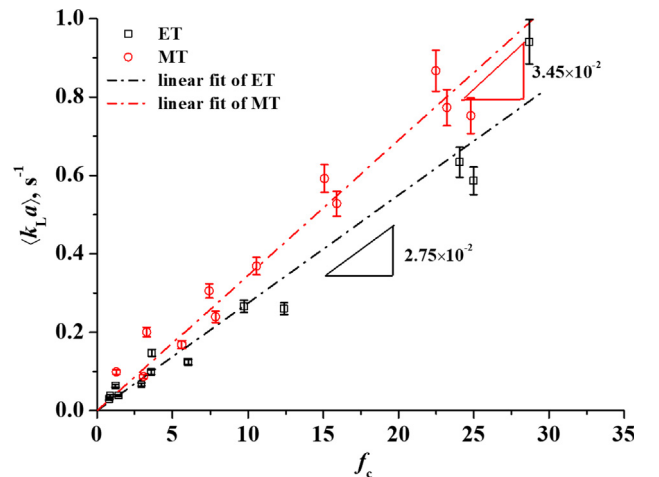


**Fig. 6.** Relations between the average overall volumetric mass transfer coefficient  $\langle k_L \cdot a \rangle$  and the frequency of circulations  $f_c$ .

$$E_{De} = \frac{\omega_{MT}}{\omega_{ET}} \quad (12)$$

The linear dimensionless coefficients for ET and MT were found to be equal to  $2.75 \times 10^{-2}$  and  $3.45 \times 10^{-2}$ , respectively, thus leading to an  $E_{De}$  of 1.25. In addition, the average square root of the inverse of the average curvature ratio increased 1.31 times from ET to MT (i.e.,  $\sqrt{\frac{1}{\langle \lambda \rangle_{MT}}} / \sqrt{\frac{1}{\langle \lambda \rangle_{ET}}} = 1.31$ ). This finding would suggest that the intensification factor for mass transfer between the two curvature ratio configurations was almost proportional to the increase of  $\sqrt{\frac{1}{\langle \lambda \rangle}}$  (the relative error is 5%), such that:

$$E_{De} = \frac{\langle k_L \cdot a \rangle_{MT}}{\langle k_L \cdot a \rangle_{ET}} \approx \sqrt{\frac{\langle \lambda \rangle_{ET}}{\langle \lambda \rangle_{MT}}} \quad (13)$$

This result is consistent with the linear relation found by Tan et al. (2012), showing that the intensification of the mass transfer coefficients was closely related to the curvature ratio.

Finally, it can be observed that the present  $\langle k_L \cdot a \rangle$  values have the same order of magnitude as those in (Roudet et al., 2011; Yang et al., 2017a). In addition, the experimental  $\langle k_L \cdot a \rangle$  were compared to the predicted  $\langle k_L \cdot a \rangle$  using literature correlations, as shown in Fig. 7. The values predicted using the correlation of Van Baten and Krishna (2004) only considered the contribution of the bubble caps, i.e.,  $\langle k_L \cdot a \rangle_{cap}$ . It can be seen that the values predicted by Bercic and Pintar (1997) and Vandu et al. (2005) are higher than the experimental data, which is quite reasonable because the present experimental data did not include the contribution from the bubble body to the liquid film. In addition, there was good agreement between the values predicted using Van Baten and Krishna (2004) and the experimental data when  $\eta$  was smaller than 2, but an underestimation when  $\eta$  was larger than 2. This can be explained by the complex flow caused by the overlap of the Taylor flow and the Dean flow for  $\eta$  greater than 2. In this case, as liquid slug lengths are half the bubble lengths, the times for one circulation are significantly decreased, leading to higher  $\langle k_L \cdot a \rangle$  compared to predicted values.

### 3.3. Axial variation of the mass flux density

The available bubble surface for mass transfer,  $S_B$ , accounting for the contribution of the liquid film or not, are assumed by two cases:

- (case S1) the liquid film around a Taylor bubble was considered, then  $S_B(X) = \frac{\pi d_B^2}{2} (1 + L_B(X)/2)$ .
- (case S2) the liquid film around the Taylor bubble was not considered, then  $S_B = \frac{\pi d_B^2}{2}$ .

The corresponding axial mass flux density  $\phi_{O_2}(X)$  was calculated for two cases respectively. The related detailed calculation is shown in the Supplementary Material. To make the mass flux density dimensionless, the Sherwood number based on the cumulated mass flux density,  $Sh$ , was introduced:

$$Sh(X) = \frac{\langle \phi_{O_2}(X) \rangle d_B(X)}{E \cdot D_{O_2} C_{O_2L}^*(X)} \quad (14)$$

where  $d_B$  is the equivalent diameter of a spherical bubble having a surface area identical to the one measured, which is also significantly dependent on the assumption made for the liquid film (see Supplementary Material).  $\langle \phi_{O_2}(X) \rangle$  is the mass flux density cumulated in the liquid slugs along the whole length of the tubing, and is intended to take former mass flux into account:

$$\langle \phi_{O_2}(X_j) \rangle = \frac{\sum_{i=1}^j \langle \phi_{O_2}(X_i) \rangle}{j}$$

$i = 1, 2, 3 \dots, j$   
 $j = 2, 3 \dots, n$

(15)

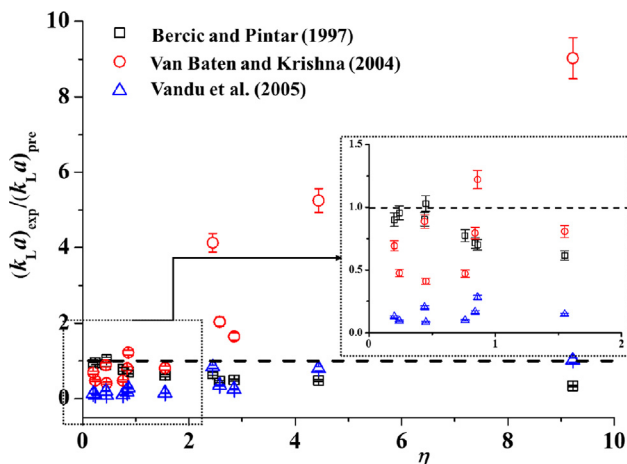


Fig. 7. Ratio between experimental  $\langle k_L \cdot a \rangle_{exp}$  and predicted  $\langle k_L \cdot a \rangle_{pre}$  versus the gas-liquid superficial velocities ratio  $\eta$ .

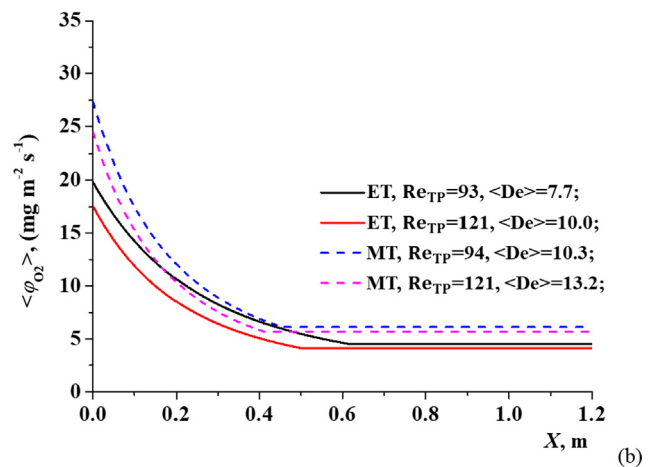
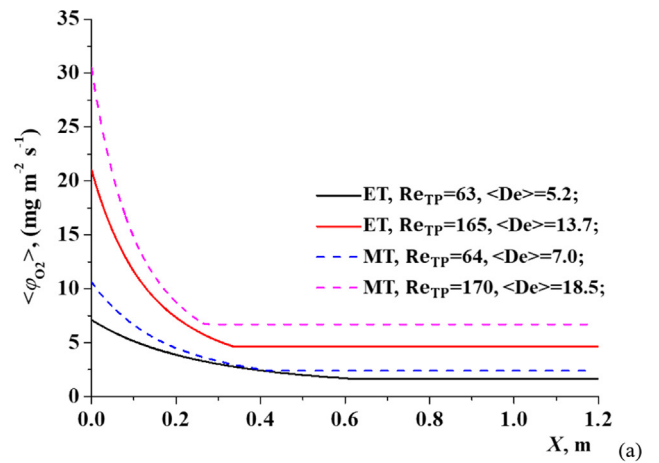


Fig. 8. Axial variation of the cumulated mass flux density  $\langle \phi_{O_2}(X) \rangle$  (case S2, without considering LF) for the tubing configurations ET and MT: (a)  $Re_L = 16.2$ ; (b)  $Re_L = 64.9$ .

where  $X_n$  represents the axial position corresponding to the fully saturated position (i.e., to  $X_{\text{coloration}}$ ). From 0 to  $X_{\text{coloration}}$ , the  $X$  axis is divided into  $n$  sections in total and the difference between adjacent axial positions is  $10^{-4}$ , i.e.,  $\Delta X = X_{i+1} - X_i = 10^{-4}$ . The subscript  $i$  varies from 1 to  $j$  and  $j$  varies from 2 to  $n$ .

Fig. 8 presents the axial variation of the cumulated mass flux density  $\langle \varphi_{O_2}(X) \rangle$  at various liquid Reynolds numbers,  $Re_L$ , for both ET and MT tubing configurations (the mass flux density here was calculated without considering LF, case S2). It can be observed that, whatever the operating condition,  $\langle \varphi_{O_2}(X) \rangle$  gradually decreases along the  $X$  and finally tends towards a constant value. A similar trend was also found in case S1 (with considering LF).

At a given  $Re_L$ ,  $\langle \varphi_{O_2}(X) \rangle$  is higher in the MT than in the ET configuration. At  $Re_L = 16.2$  and for the same configuration,  $\langle \varphi_{O_2}(X) \rangle$  increases with  $Re_{TP}$  (see Fig. 8(a)). Surprisingly, in Fig. 8 (b), at  $Re_L = 64.9$ , an opposite trend is observed. A reasonable explanation for this discrepancy may be that the decrease of  $\langle L_S \rangle$  (e.g., -44% in ET) was more pronounced compared to the increase of  $\langle U_B \rangle$  (e.g., 29% in ET).

The ‘‘intrinsic’’ Sherwood number,  $Sh$ , (i.e. the one corresponding to the physical absorption process) can be estimated from the measured apparent Sherwood number (using the resazurin colorimetric method) if the enhancement factor,  $E$ , is known. As shown by Yang et al. (2016), when the Hatta number is bigger than 3,  $E$  can be estimated by the approximate solution proposed by Van Krevelen and Hoftijzer (1948):

$$E = \frac{Ha \sqrt{(E_i - E)/(E_i - 1)}}{\tanh(Ha \sqrt{(E_i - E)/(E_i - 1)})} \quad (16)$$

where  $E_i$  and  $Ha$  are the limit enhancement factor and the Hatta number, respectively, further expressed as:

$$E_i = 1 + \frac{D_{DH} C_{DH,0}}{2D_{O_2} C_{O_2}^*} \quad (17)$$

$$Ha = \frac{\sqrt{k_2 C_{DH,0} D_{O_2}}}{k_L} \quad (18)$$

where the liquid side mass transfer coefficient,  $k_L$ , can be deduced using the measured Sherwood number  $Sh$ :

$$k_L = \frac{Sh \cdot D_{O_2}}{d_B(X)} = \frac{\langle \varphi_{O_2}(X) \rangle}{E \cdot C_{O_{2L}}(X)} \quad (19)$$

Therefore, from Eqs. (16) to (19),  $Ha$  and  $E$  can be calculated by solving the following two implicit equations:

$$E = \frac{Ha \sqrt{\left(1 + \frac{D_{DH} C_{DH,0}}{2D_{O_2} C_{O_2}^*} - E\right) / \left(1 + \frac{D_{DH} C_{DH,0}}{2D_{O_2} C_{O_2}^*} - 1\right)}}{\tanh\left(Ha \sqrt{\left(1 + \frac{D_{DH} C_{DH,0}}{2D_{O_2} C_{O_2}^*} - E\right) / \left(1 + \frac{D_{DH} C_{DH,0}}{2D_{O_2} C_{O_2}^*} - 1\right)}\right)} \quad (20)$$

$$Ha = \frac{E \cdot C_{O_{2L}}(X) \sqrt{k_2 C_{DH,0} D_{O_2}}}{\langle \varphi_{O_2}(X) \rangle} \quad (21)$$

The reaction rate constant  $k_2$  of  $1.28 \times 10^6 \text{ L mol}^{-1} \text{ s}^{-1}$  found by Yang et al. (2016) was adopted.

- (case S1) The Hatta numbers were found to be greater than 5 for all operating cases, both in ET and MT, and the enhancement factor ranged from 1.07 to 1.08;
- (case S2) When the Hatta numbers ranged between 3 and 17, the enhancement factors were between 1.05 and 1.07 and, when  $Ha$  ranged from 0.3 to 3 for other operating conditions,  $E$  tended towards to unity.

Thus, from these calculations, the overestimation of the Sherwood number caused by chemical reaction (oxidation of DH to RF) was below 10% for all conditions and was neglected in the next section.

### 3.4. Scaling laws for the cumulated Sherwood number

The former variation was described using dimensional parameters, i.e.,  $\langle \varphi_{O_2}(X) \rangle$ . In a first attempt to group all the experimental data in a single master curve, the Sherwood number and a normalized time  $t^*$  defined from the coloration time were introduced:

$$t^* = \frac{t}{t_{\text{coloration}}} = \frac{X}{\langle U_B \rangle t_{\text{coloration}}} = \frac{X}{4N_{\text{circulation}} \langle L_S \rangle} \quad (22)$$

where  $N_{\text{circulation}}$  is defined as the number of circulation loops needed to reach the full coloration time:

$$N_{\text{circulation}} = \frac{t_{\text{coloration}}}{t_{\text{circulation}}} = \frac{t_{\text{coloration}}}{4\langle L_S \rangle / \langle U_B \rangle} \quad (23)$$

the average numbers  $N_{\text{circulation}}$  for ET and MT are found to be  $32.7 \pm 4.4$  and  $26.1 \pm 3.1$ , respectively. The cumulated Sherwood number can be calculated with Eq. (14), in which the enhancement factor,  $E$ , is considered as the unit.

In addition, the Péclet number,  $Pe$ , was introduced to evaluate the effect of the ratio between the advective transport and diffusive transport rates:

$$Pe = \langle Re_B \rangle Sc \quad (24)$$

where  $Sc$  is the Schmidt number, defined as  $Sc = \frac{\mu}{\rho_L D_{O_2}}$ , fixed in the present study at 348.  $Re_B$  is the bubble Reynolds number, defined here as  $\langle Re_B \rangle = \frac{\rho_L \langle U_B \rangle d_B}{\mu_L}$ . To evaluate the effects of centrifugal force, the average Dean number, defined from  $\langle De_B \rangle = \langle Re_B \rangle \sqrt{\frac{1}{\langle \bar{r} \rangle}}$ , was also considered.

A scaling-law is thus proposed to separate the developing zone (entrance effect) from the fully-developed zone by the normalized time  $t^*$ . This function is expressed as

- for  $t^* \geq 1$  (fully-developed zone):

$$Sh(t^*) = W_1 Pe^{0.5} \langle De_B \rangle \frac{\langle L_S \rangle}{d_{it}} \quad (25)$$

- for  $t^* < 1$  (entrance zone):

$$Sh(t^*) = W_2 Pe^{0.5} \langle De_B \rangle \frac{\langle L_S \rangle}{d_{it}} e^{-W_3 t^*} (1 - t^*) + W_1 Pe^{0.5} \langle De_B \rangle \frac{\langle L_S \rangle}{d_{it}} \quad (26)$$

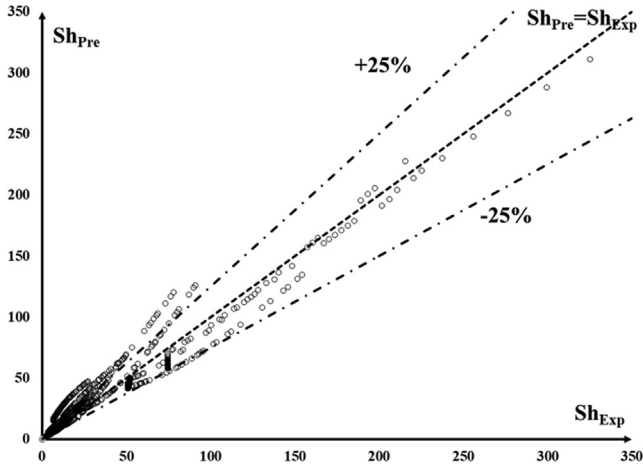
where the exponential coefficient of  $Pe$  is fixed at 0.5, as verified by previous researchers (Kastens et al., 2015; Roudet et al., 2017; Yang, 2017).

All the experimental data obtained for ET and MT (25 operating conditions in total) were regressed by the nonlinear model in MATLAB and two cases (cases S1 and S2) were considered. The regressed coefficients are listed in Table 1, according to whether the liquid film is (case S1) or is not (case S2) considered. It can be seen from Table 1 that  $W_1$  and  $W_2$  in case S2 were almost 5 and 4 times higher than those in S1. Such differences confirm the importance of the liquid film contribution in the whole mass transfer. It was found that this scaling law enabled all the Sherwood numbers for both tubing configurations to be grouped together. In Fig. 9, the predicted and experimental Sherwood numbers are

**Table 1**

Regressed dimensionless coefficients of scaling laws for ET and MT.

Case	Configuration	$W_1 \times 10^3$	$W_2 \times 10^3$	$W_3$	$N_{\text{circulation}}$	STD
S1 (with LF)	ET	2.14	6.96	1.90	32.7	23%
	MT				26.1	17%
S2 (without LF)	ET	10.78	30.68	2.01	32.7	25%
	MT				26.1	20%

**Fig. 9.** Comparison between the predicted  $Sh_{\text{pre}}$  and experimental  $Sh_{\text{exp}}$  in case S2 (without LF) for ET configuration.

compared using the worst conditions, i.e., highest standard deviation (i.e., case S2 in ET). It can be seen that the scaling law performs well for  $Sh > 100$ . When  $Sh < 100$ , the deviation becomes larger, which corresponds to some extreme conditions, e.g., when the liquid slug length  $L_S$  is very long and  $Re_B$  is very small. Under this condition, the circulation time is quite long and deviation from the assumption of perfect mixing in the liquid slug is high. The proposed  $Sh$  scaling law thus leads to an overestimation.

This first attempt of proposing a scaling law has the advantage of revealing and dissociating the entrance effects and steady state during mass transfer process. Eq. (25) represents the fully developed mass transfer state, obtained far from the T-junction, where the Sherwood number does not depend on the dimensionless time (i.e. on the axial position). The corresponding fully established Sherwood number, noted  $Sh_{\infty}$ , is then proportional to  $Pe^{0.5}$ ,  $\langle De_B \rangle$  and  $\langle L_S \rangle / d_{it}$ . Therefore,  $Sh_{\infty}$  is higher in MT than ET due to a higher  $\langle De_B \rangle$ .

The entrance effect is represented by the first term in Eq. (26), corresponding to the initial time at bubble formation (i.e.,  $(W_1 + W_2)Pe^{0.5} \langle De_B \rangle \langle L_S \rangle / d_{it}$ ). It can be deduced that the entrance effect was affected by centrifugal forces for both cases, and was proportional to  $\langle De_B \rangle$ . The time required to reach the steady state was smaller for MT than ET, because a lower number of circulation loops,  $N_{\text{circulation}}$ , was needed to achieve the steady state in MT. This would suggest that the mass transfer dynamics were closely related to the circulation intensities and also to the induced Dean flow (Zaloha et al., 2012).

#### 4. Conclusions

The aim of this original experimental study was to investigate the overall and cumulated gas-liquid mass transfer around Taylor bubbles (air) in an in-plane, spiral-shaped milli-reactor. Using the resazurin-based colorimetric technique and image processing, the axial variation of equivalent  $O_2$  concentration in liquid slugs was

experimentally characterized over a long distance inside the milli-reactor.

The main findings were the following:

- 1) Average overall volumetric mass transfer coefficients  $\langle k_L a \rangle$  could be easily and directly acquired through the coloration position. They increased linearly with circulation frequency  $f_c$ , which would suggest that the mass transfer was closely related to the circulation loops (i.e.,  $\langle U_B \rangle$  and  $\langle L_S \rangle$ ). The intensification factor  $E_{De}$  (1.25) for  $\langle k_L a \rangle$  was found to be almost identical to the increase of the average Dean number (1.31) from the ET configurations to MT.
- 2) Considering the pressure drop, bubble expansion and bubble velocity increase, the axial variation of cumulated mass flux density  $\langle \varphi_{O_2}(X) \rangle$  was deduced. It was found that  $\langle \varphi_{O_2}(X) \rangle$  gradually decreased with the axial position and finally tended towards a constant value.
- 3) Finally, the cumulated Sherwood number was correlated with a normalized time (depending on the circulation time), dimensionless liquid slug length, Péclet number and Dean number. A scaling law was proposed for both ET and MT configurations, and was established according to whether the liquid film was considered or not in the modeling, which could enable the entrance effects to be dissociated from the steady state of mass transfer.

All these findings could provide important information for implementing gas-liquid mass transfer in continuous-flow reactors. Future studies will need to focus on the contribution of the liquid film to the mass transfer and further investigate the entrance effects.

#### CRedit authorship contribution statement

**Mei Mei:** Conceptualization, Methodology, Software, Validation, Investigation, Data curation, Writing - original draft, Writing - review & editing, Visualization. **Gilles Hébrard:** Conceptualization, Methodology, Validation, Writing - review & editing, Funding acquisition, Supervision, Project administration. **Nicolas Dietrich:** Conceptualization, Methodology, Validation, Writing - review & editing, Funding acquisition, Supervision, Project administration. **Karine Loubière:** Conceptualization, Methodology, Validation, Writing - review & editing, Funding acquisition, Supervision, Project administration.

#### Declaration of Competing Interest

The authors declare that they have no known competing financial interests or personal relationships that could have appeared to influence the work reported in this paper.

#### Acknowledgments

The authors would like to acknowledge the financial assistance provided by the China Scholarship Council. We also acknowledge

the support for this work received from the CNRS research federation FERMaT.

## Appendix A. Supplementary material

Supplementary data to this article can be found online at <https://doi.org/10.1016/j.ces.2020.115717>.

## References

- Abiev, R.S., Butler, C., Cid, E., Lalanne, B., Billet, A.M., 2019. Mass transfer characteristics and concentration field evolution for gas-liquid Taylor flow in milli channels. *Chem. Eng. Sci.* <https://doi.org/10.1016/j.ces.2019.07.046>.
- Abiev, Rufat, Svetlov, S., Haase, S., 2017. Hydrodynamics and mass transfer of gas-liquid and liquid-liquid Taylor flow in micro channels: a review. *Chem. Eng. Technol.* <https://doi.org/10.1002/ceat.201700041>.
- Aillet, T., Loubière, K., Dechy-Cabaret, O., Prat, L., 2016. Microreactors as a tool for acquiring kinetic data on photochemical reactions. *Chem. Eng. Technol.* 39, 115–122. <https://doi.org/10.1002/ceat.201500163>.
- Benizri, D., Dietrich, N., Labeyrie, P., Hébrard, G., 2019. A compact, economic scrubber to improve farm biogas upgrading systems. *Sep. Purif. Technol.* 219, 169–179. <https://doi.org/10.1016/j.seppur.2019.02.054>.
- Bercic, G., Pintar, A., 1997. The role of gas bubbles and liquid slug lengths on mass transport in the Taylor flow through capillaries. *Chem. Eng. Sci.* 52, 3709–3719. [https://doi.org/10.1016/S0009-2509\(97\)00217-0](https://doi.org/10.1016/S0009-2509(97)00217-0).
- Butler, C., Cid, E., Billet, A.M., 2016. Modelling of mass transfer in Taylor flow: investigation with the PLIF-1 technique. *Chem. Eng. Res. Des.* 115, 292–302. <https://doi.org/10.1016/j.cherd.2016.09.001>.
- Butler, C., Lalanne, B., Sandmann, K., Cid, E., Billet, A.M., 2018. Mass transfer in Taylor flow: transfer rate modelling from measurements at the slug and film scale. *Int. J. Multiph. Flow* 105, 185–201. <https://doi.org/10.1016/j.ijmultiphaseflow.2018.04.005>.
- Dietrich, N., Hébrard, G., 2018. Visualisation of gas-liquid mass transfer around a rising bubble in a quiescent liquid using an oxygen sensitive dye. *Heat Mass Transf.* 1–9.
- Dietrich, N., Loubière, K., Jimenez, M., Hébrard, G., Gourdon, C., 2013. A new direct technique for visualizing and measuring gas-liquid mass transfer around bubbles moving in a straight millimetric square channel. *Chem. Eng. Sci.* 100, 172–182. <https://doi.org/10.1016/j.ces.2013.03.041>.
- Dietrich, N., Wongwailikhit, K., Mei, M., Xu, F., Felis, F., Kherbeche, A., Hébrard, G., Loubière, K., 2019. Using the “red bottle” experiment for the visualization and the fast characterization of gas-liquid mass transfer. *J. Chem. Educ.* 96, 979–984. <https://doi.org/10.1021/acs.jchemed.8b00898>.
- Eskin, D., Mostowfi, F., 2012. A model of a bubble train flow accompanied with mass transfer through a long microchannel. *Int. J. Heat Fluid Flow* 33, 147–155. <https://doi.org/10.1016/j.ijheatfluidflow.2011.11.001>.
- Fries, D.M., von Rohr, P.R., 2009. Liquid mixing in gas-liquid two-phase flow by meandering microchannels. *Chem. Eng. Sci.* 64, 1326–1335. <https://doi.org/10.1016/j.ces.2008.11.019>.
- García-Ochoa, F., Gomez, E., Santos, V.E., Merchuk, J.C., 2010. Oxygen uptake rate in microbial processes: an overview. *Biochem. Eng. J.* 49, 289–307. <https://doi.org/10.1016/j.bej.2010.01.011>.
- Ghobadi, M., Muzychka, Y.S., 2013. Effect of entrance region and curvature on heat transfer in mini scale curved tubing at constant wall temperature. *Int. J. Heat Mass Transf.* 65, 357–365. <https://doi.org/10.1016/j.ijheatmasstransfer.2013.05.078>.
- Gourdon, C., Elgue, S., Prat, L., 2015. What are the needs for process intensification?. *Oil & Gas Sci. Technol.-Revue d'IFP Energies nouvelles* 70, 463–473. <https://doi.org/10.2516/ogst/2014051>.
- Guo, Liejin, Chen, Y., Su, J., Liu, M., Liu, Y., 2019. Obstacles of solar-powered photocatalytic water splitting for hydrogen production: a perspective from energy flow and mass flow. *Energy* 172, 1079–1086. <https://doi.org/10.1016/j.energy.2019.02.050>.
- Guo, Lin, Liu, W., Tang, X., Wang, H., Liu, Q., Zhu, Y., 2017. Reaction kinetics of non-catalyzed jet aeration oxidation of magnesium sulfite. *Chem. Eng. J.* 330, 870–879. <https://doi.org/10.1016/j.cej.2017.07.169>.
- Haase, S., Murzin, D.Y., Salmi, T., 2016. Review on hydrodynamics and mass transfer in minichannel wall reactors with gas-liquid Taylor flow. *Chem. Eng. Res. Des.* 113, 304–329. <https://doi.org/10.1016/j.cherd.2016.06.017>.
- Hosoda, S., Abe, S., Hosokawa, S., Tomiyama, A., 2014. Mass transfer from a bubble in a vertical pipe. *Int. J. Heat Mass Transf.* 69, 215–222. <https://doi.org/10.1016/j.ijheatmasstransfer.2013.10.031>.
- Jensen, K.F., 2001. Microreaction engineering—is small better?. *Chem. Eng. Sci.* 56, 293–303. [https://doi.org/10.1016/S0009-2509\(00\)00230-X](https://doi.org/10.1016/S0009-2509(00)00230-X).
- Kastens, S., Hosoda, S., Schlueter, M., Tomiyama, A., 2015. Mass transfer from single Taylor bubbles in minichannels. *Chem. Eng. Technol.* 38, 1925–1932. <https://doi.org/10.1002/ceat.201500065>.
- Kherbeche, A., Mei, M., Thoraval, M.-J., Hébrard, G., Dietrich, N., 2019. Hydrodynamics and gas-liquid mass transfer around a confined sliding bubble. *Chem. Eng. J.* <https://doi.org/10.1016/j.cej.2019.04.041>.
- Kherbeche, A., Milnes, J., Jimenez, M., Dietrich, N., Hébrard, G., Lekhlif, B., 2013. Multi-scale analysis of the influence of physicochemical parameters on the hydrodynamic and gas-liquid mass transfer in gas/liquid/solid reactors. *Chem. Eng. Sci.* 100, 515–528. <https://doi.org/10.1016/j.ces.2013.06.025>.
- Kováts, P., Pohl, D., Thévenin, D., Zähringer, K., 2018. Optical determination of oxygen mass transfer in a helically-coiled pipe compared to a straight horizontal tube. *Chem. Eng. Sci.* 190, 273–285. <https://doi.org/10.1016/j.ces.2018.06.029>.
- Krieger, W., Bayraktar, E., Mierka, O., Kaiser, L., Dinter, R., Hennekes, J., Turek, S., Kockmann, N., 2020. Arduino-based slider setup for gas-liquid mass transfer investigations: experiments and CFD simulations. *AIChE J.* <https://doi.org/10.1002/aic.16953>.
- Krieger, W., Hörbelt, M., Schuster, S., Hennekes, J., Kockmann, N., 2019. Kinetic study of leuco-indigo carmine oxidation and investigation of Taylor and Dean flow superposition in a coiled flow inverter. *Chem. Eng. Technol.* <https://doi.org/10.1002/ceat.201800753>.
- Krieger, W., Lamsfuß, J., Zhang, W., Kockmann, N., 2017. Local mass transfer phenomena and chemical selectivity of gas-liquid reactions in capillaries. *Chem. Eng. Technol.* 40, 2134–2143. <https://doi.org/10.1002/ceat.201700420>.
- Kuhn, S., Jensen, K.F., 2012. A pH-sensitive laser-induced fluorescence technique to monitor mass transfer in multiphase flows in microfluidic devices. *Ind. Eng. Chem. Res.* 51, 8999–9006. <https://doi.org/10.1021/ie300978n>.
- Kurt, S.K., Warnebold, F., Nigam, K.D.P., Kockmann, N., 2017. Gas-liquid reaction and mass transfer in microstructured coiled flow inverter. *Chem. Eng. Sci.* <https://doi.org/10.1016/j.ces.2017.01.017>.
- Liu, Y., Yue, J., Xu, C., Zhao, S., Yao, C., Chen, G., 2020. Hydrodynamics and local mass transfer characterization under gas-liquid-liquid slug flow in a rectangular microchannel. *AIChE J.* 66. <https://doi.org/10.1002/aic.16805> e16805.
- Loubière, K., G.F., Radjagobalou R., P.A.B.J.-F., Elgue S., Prat L., Dechy-Cabaret O., 2017. LED-driven spiral-shaped microreactor as a tool to investigate sensitized photooxygenations. *European Photochemistry Association (EPA) Newsletters Special Issue “Synthetic Organic Photochemistry”* 93, 42–46. <https://doi.org/10.1007/s10404-017-1896-5>.
- Mei, M., Felis, F., Dietrich, N., Hébrard, G., Loubière, L., 2020. Hydrodynamics of gas-liquid slug flows in a long in-plane spiral-shaped milli-reactor. *Theor. Found. Chem. Eng.* 54, 25–47. <https://link.springer.com/article/10.1134/S0040579520010169>.
- Nirmal, G.M., Leary, T.F., Ramachandran, A., 2019. Mass transfer dynamics in the dissolution of Taylor bubbles. *Soft Matter* 15, 2746–2756. <https://doi.org/10.1039/C8SM01144C>.
- Pan, Z., Zhang, X., Xie, Y., Cai, W., 2014. Instantaneous mass transfer under gas-liquid Taylor flow in circular capillaries. *Chem. Eng. Technol.* 37, 495–504. <https://doi.org/10.1002/ceat.201300354>.
- Paul, M., Strassl, F., Hoffmann, A., Hoffmann, M., Schlüter, M., Herres-Pawlis, S., 2018. Reaction systems for bubbly flows. *Eur. J. Inorg. Chem.* 2018, 2101–2124. <https://doi.org/10.1002/ejic.201800146>.
- Radjagobalou, R., Blanco, J.-F., Dechy-Cabaret, O., Oelgemöller, M., Loubière, K., 2018. Photooxygenation in an advanced led-driven flow reactor module: Experimental investigations and modelling. *Chem. Eng. Process. - Process Intensif.* 130, 214–228. <https://doi.org/10.1016/j.cep.2018.05.015>.
- Roudet, M., Billet, A.M., Cazin, S., Risso, F., Roig, V., 2017. Experimental investigation of interfacial mass transfer mechanisms for a confined high-reynolds-number bubble rising in a thin gap. *AIChE J.* 63, 2394–2408. <https://doi.org/10.1002/aic.15562>.
- Roudet, M., Loubiere, K., Gourdon, C., Cabassud, M., 2011. Hydrodynamic and mass transfer in inertial gas-liquid flow regimes through straight and meandering millimetric square channels. *Chem. Eng. Sci.* 66, 2974–2990. <https://doi.org/10.1016/j.ces.2011.03.045>.
- Sattari-Najafabadi, M., Nasr Esfahany, M., Wu, Z., Sunden, B., 2018. Mass transfer between phases in microchannels: a review. *Chem. Eng. Process. - Process Intensif.* 127, 213–237. <https://doi.org/10.1016/j.cep.2018.03.012>.
- Sobieszuk, P., Aubin, J., Pohorecki, R., 2012. Hydrodynamics and mass transfer in gas-liquid flows in microreactors. *Chem. Eng. Technol.* 35, 1346–1358. <https://doi.org/10.1002/ceat.201100643>.
- Stankiewicz, A., Van Gerven, T., Stefanidis, G., 2019. *The Fundamentals of Process Intensification*. John Wiley & Sons.
- Svetlov, S., Abiev, R.S., 2016. Modeling mass transfer in a Taylor flow regime through microchannels using a three-layer model. *Theor. Found. Chem. Eng.* 50, 975–989. <https://doi.org/10.1134/S0040579516060166>.
- Tan, J., Lu, Y.C., Xu, J.H., Luo, G.S., 2012. Mass transfer performance of gas-liquid segmented flow in microchannels. *Chem. Eng. J.* 181, 229–235. <https://doi.org/10.1016/j.cej.2011.11.067>.
- Van Baten, J., Krishna, R., 2004. CFD simulations of mass transfer from Taylor bubbles rising in circular capillaries. *Chem. Eng. Sci.* 59, 2535–2545. <https://doi.org/10.1016/j.ces.2004.03.010>.
- Van Hecke, W., Bockrath, R., De Wever, H., 2019. Effects of moderately elevated pressure on gas fermentation processes. *Bioresour. Technol.* 293. <https://doi.org/10.1016/j.biortech.2019.122129> 122129.
- Van Krevelen, D., Hofstijzer, P., 1948. Kinetics of gas-liquid reactions part I. General theory. *Recl. Trav. Chim. Pays-Bas* 67, 563–586. <https://doi.org/10.1002/recl.19480670708>.
- Vandu, C.O., Liu, H., Krishna, R., 2005. Mass transfer from Taylor bubbles rising in single capillaries. *Chem. Eng. Sci.* 60, 6430–6437. <https://doi.org/10.1016/j.ces.2005.01.037>.
- Vashisth, S., Kumar, V., Nigam, K.D., 2008. A review on the potential applications of curved geometries in process industry. *Ind. Eng. Chem. Res.* 47, 3291–3337. <https://doi.org/10.1021/ie701760h>.

- Yang, L., 2017. Local investigations of gas-liquid mass transfer around Taylor bubbles flowing in straight and meandering millimetric channels using a colorimetric method PhD thesis. University of Toulouse, INSA.
- Yang, L., Dietrich, N., Loubière, K., Gourdon, C., Hébrard, G., 2016. Optical methods to investigate the enhancement factor of an oxygen-sensitive colorimetric reaction using microreactors. *AIChE J.* <https://doi.org/10.1002/aic.15547>.
- Yang, L., Loubière, K., Dietrich, N., Men, C.L., Gourdon, C., Hébrard, G., 2017a. Local investigations on the gas-liquid mass transfer around Taylor bubbles flowing in a meandering millimetric square channel. *Chem. Eng. Sci.* 165, 192–203. <https://doi.org/10.1016/j.ces.2017.03.007>.
- Yang, L., Nieves-Remacha, M.J., Jensen, K.F., 2017b. Simulations and analysis of multiphase transport and reaction in segmented flow microreactors. *Chem. Eng. Sci.* 169, 106–116. <https://doi.org/10.1016/j.ces.2016.12.003>.
- Yao, C., Dong, Z., Zhao, Y., Chen, G., 2014. An online method to measure mass transfer of slug flow in a microchannel. *Chem. Eng. Sci.* 112, 15–24. <https://doi.org/10.1016/j.ces.2014.03.016>.
- Yao, C., Zhao, Y., Zheng, J., Zhang, Q., Chen, G., 2020. The effect of liquid viscosity and modeling of mass transfer in gas-liquid slug flow in a rectangular microchannel. *AIChE J.*, e16934 <https://doi.org/10.1002/aic.16934>.
- Yin, Y., Fu, T., Zhu, C., Guo, R., Ma, Y., Li, H., 2018. Dynamics and mass transfer characteristics of CO<sub>2</sub> absorption into MEA/[Bmim][BF<sub>4</sub>] aqueous solutions in a microchannel. *Sep. Purif. Technol.* <https://doi.org/10.1016/j.seppur.2018.08.045>.
- Yue, J., 2017. Multiphase flow processing in microreactors combined with heterogeneous catalysis for efficient and sustainable chemical synthesis. *Catal. Today.* <https://doi.org/10.1016/j.cattod.2017.09.041>.
- Yue, J., Chen, G., Yuan, Q., Luo, L., Gonthier, Y., 2007. Hydrodynamics and mass transfer characteristics in gas-liquid flow through a rectangular microchannel. *Chem. Eng. Sci.* 62, 2096–2108. <https://doi.org/10.1016/j.ces.2006.12.057>.
- Zaloha, P., Kristal, J., Jiricny, V., Völkel, N., Xuereb, C., Aubin, J., 2012. Characteristics of liquid slugs in gas-liquid Taylor flow in microchannels. *Chem. Eng. Sci.* 68, 640–649. <https://doi.org/10.1016/j.ces.2011.10.036>.
- Zhang, Peng, Yao, C., Ma, H., Jin, N., Zhang, X., Lü, H., Zhao, Y., 2018. Dynamic changes in gas-liquid mass transfer during Taylor flow in long serpentine square microchannels. *Chem. Eng. Sci.* <https://doi.org/10.1016/j.ces.2018.02.018>.
- Zhang, Weipeng, Wang, X., Feng, X., Yang, C., Mao, Z.-S., 2016. Investigation of Mixing Performance in Passive Micromixers. *Ind. Eng. Chem. Res.* 55, 10036–10043. <https://doi.org/10.1021/acs.iecr.6b01765>.

## Supplementary Material

### *Gas-liquid mass transfer around Taylor bubbles flowing in a long in-plane spiral-shaped milli-reactor*

Mei Mei, Gilles Hébrard, Nicolas Dietrich, Karine Loubière\*

#### 1. Operating conditions and main hydrodynamics results for ET and MT configurations

**Table S1.** Experimental results of gas-liquid hydrodynamics in the ET configuration

$j_L$ cm s <sup>-1</sup>	$j_G$ cm s <sup>-1</sup>	$\eta$ (-)	Re <sub>L</sub> (-)	Re <sub>G</sub> (-)	Re <sub>TP</sub> (-)	$\langle De \rangle$ (-)	$\langle U_B \rangle$ cm s <sup>-1</sup>	$\langle L_B \rangle$ mm	$\langle L_S \rangle$ mm	$F_1$ (-)	$L_{B0}$ mm	$F_2 \times 10^{-3}$ s <sup>-1</sup>	$U_{B0}$ cm s <sup>-1</sup>	$F_3$ Pa m <sup>-1</sup>	$p_{B0} \times 10^5$ Pa
1.80	0.82	0.45	16.2	0.9	24	2.0	2.70	6.34	8.43	0.61	5.53	0.90	2.58	-0.11	1.34
1.80	1.08	0.60	16.2	1.2	26	2.2	3.02	7.18	6.58	0.82	6.11	1.45	2.82	-0.13	1.42
1.80	1.37	0.76	16.2	1.5	28	2.3	3.30	8.14	5.83	1.05	6.74	2.13	3.15	-0.16	1.48
1.80	2.79	1.55	16.2	3.0	41	3.4	5.28	12.15	4.47	1.11	10.45	2.96	4.62	-0.11	1.33
1.80	5.13	2.85	16.2	5.5	63	5.2	8.63	18.92	3.58	1.31	16.27	4.13	7.34	-0.08	1.26
1.80	16.60	9.22	16.2	17.9	165	13.7	21.78	40.35	2.18	1.94	37.52	8.58	19.1	-0.05	1.17
3.61	0.87	0.24	32.4	0.9	40	3.3	4.23	5.04	12.06	0.50	4.34	1.00	4.49	-0.12	1.36
3.61	3.04	0.84	32.4	3.3	60	5.0	7.21	8.39	5.01	1.02	7.00	4.43	6.56	-0.15	1.45
3.61	9.30	2.58	32.4	10.0	116	9.6	15.12	15.10	3.05	1.18	13.49	8.13	13.28	-0.09	1.28
3.61	16.02	4.44	32.4	17.3	176	14.6	23.19	21.25	2.41	1.43	19.35	11.84	20.05	-0.07	1.24
7.22	1.41	0.20	64.9	1.5	78	6.5	7.84	4.54	15.94	0.37	4.04	1.29	8.64	-0.09	1.29
7.22	3.16	0.44	64.9	3.4	93	7.7	10.14	5.49	6.95	0.70	4.55	4.86	10.42	-0.15	1.48
7.22	6.22	0.86	64.9	6.7	121	10.0	14.93	7.01	3.84	1.00	5.68	10.95	13.69	-0.18	1.54
7.22	17.68	2.45	64.9	19.1	224	18.6	27.30	11.74	2.38	1.22	10.14	21.27	25.2	-0.12	1.37

**Table S2.** Experimental results of gas-liquid hydrodynamics in the MT configuration

$j_L$ , cm s <sup>-1</sup>	$j_G$ , cm s <sup>-1</sup>	$\eta$ (-)	Re <sub>L</sub> , (-)	Re <sub>G</sub> , (-)	Re <sub>TP</sub> , (-)	$\langle De \rangle$ , (-)	$\langle U_B \rangle$ , cm s <sup>-1</sup>	$\langle L_B \rangle$ , mm	$\langle L_S \rangle$ , mm	$F_1$ , (-)	$L_{B0}$ , mm	$F_2 \times 10^{-3}$ , (s <sup>-1</sup> )	$U_{B0}$ , cm s <sup>-1</sup>	$F_3$ , Pa m <sup>-1</sup>	$p_{B0} \times 10^5$ , Pa
1.80	1.09	0.61	16.2	1.2	26	2.8	2.91	5.91	6.40	0.87	4.86	1.95	2.73	-0.18	1.54
1.80	3.19	1.77	16.2	3.4	45	4.9	5.02	10.10	4.06	0.84	9.07	2.95	4.76	-0.09	1.29
1.80	5.32	2.96	16.2	5.7	64	7.0	7.94	15.59	3.53	1.21	14.09	4.57	7.56	-0.09	1.27
1.80	7.14	3.97	16.2	7.7	80	8.7	10.12	19.88	3.23	1.30	18.25	5.09	9.74	-0.07	1.22
1.80	17.13	9.52	16.2	18.5	170	18.5	22.43	35.12	2.26	1.34	33.26	6.90	21.46	-0.04	1.13
3.61	1.37	0.38	32.4	1.5	45	4.9	4.62	4.77	8.94	0.70	3.91	2.45	4.39	-0.18	1.54
3.61	9.33	2.58	32.4	10.1	116	12.7	14.07	12.95	3.33	1.13	11.56	9.12	12.99	-0.10	1.30
3.61	12.37	3.43	32.4	13.3	144	15.7	18.18	15.50	2.86	1.18	14.05	10.39	16.95	-0.08	1.26
3.61	16.29	4.51	32.4	17.6	179	19.5	22.93	18.28	2.47	1.27	16.68	12.40	21.78	-0.08	1.24
7.22	3.30	0.46	64.9	3.6	94	10.3	10.16	4.91	7.68	0.55	4.24	4.28	9.60	-0.13	1.39
7.22	6.24	0.86	64.9	6.7	121	13.2	13.99	6.57	4.72	0.99	5.36	11.53	12.67	-0.18	1.56
7.22	11.53	1.60	64.9	12.4	168	18.3	20.45	8.40	3.39	1.06	7.10	17.21	18.61	-0.15	1.45
7.22	15.37	2.13	64.9	16.6	203	22.1	25.63	9.58	2.85	1.16	8.14	21.90	22.76	-0.14	1.43

The linear axial evolution of bubble length, velocity and pressure are expressed as below:

$$L_B(X) = F_1 X + L_{B0}, \quad (\text{SI.1})$$

$$U_B(X) = F_2 X + U_{B0}, \quad (\text{SI.2})$$

$$p_B(X) = F_3 X + p_{B0}, \quad (\text{SI.3})$$

where  $F_1$ ,  $F_2$  and  $F_3$  refer to the slopes of the straight lines related to bubble length, velocity and pressure with axial location  $X$ ;  $L_{B0}$ ,  $U_{B0}$  and  $p_{B0}$  are the initial bubble length, velocity and pressure, i.e. the ones immediately after the bubble forms. By using the image processing and the least squares regression method, all the slopes and initial values at  $X=0$  were calculated and are listed in Tables S1 and S2 for each operating

condition.

## 2. Comparison of global and pixel-by-pixel calibrations

In Fig. S1, the profiles of equivalent  $O_2$  concentration along the  $\Gamma_Y$  line (see Fig. 1 (b)) are compared, depending whether a pixel-by-pixel method or a global method was used for calibration. For the pixel-by-pixel calibration, the linear regressions of equivalent  $O_2$  concentration and  $\Delta G$  were implemented for each pixel inside the tube on the image, meaning that the  $\Delta G$  was calculated for each pixel. For the global calibration, the linear regression of equivalent  $O_2$  concentration and  $\Delta G$  was only applied once for all the pixels inside the tube on the image, so  $\Delta G$  is an average value for all the pixels on the image. The spiral turn numbers along the  $\Gamma_Y$  line were labeled as 1 to 11 from top to bottom as shown in Fig. 1 (b).

The slight variations in gray values observed at different tubing positions could be caused by the inhomogeneous light distribution and the complex tubing conditions. One can see that the equivalent  $O_2$  concentrations obtained by global calibration at a given RZ concentration were scattered (the maximum relative error was 15%) and varied for different spiral numbers. However, the ones using pixel-by-pixel calibration at a given RZ concentration remained uniform (the maximum relative error was 6%) whatever the tubing position. For each spiral turn, the error bar represents the standard deviation for all pixels along the  $\Gamma_Y$  direction belonging to this spiral tube turn.

In addition, the obtained maximum equivalent  $O_2$  concentration  $C_{\max}$  (named “concentration 5” on Fig. S1) was found close to  $6.5 \text{ mg L}^{-1}$ , instead of the expected  $7.33 \text{ mg L}^{-1}$  (corresponding to the  $0.105 \text{ g L}^{-1}$  RZ, calculated from the chemical stoichiometry of DH and  $O_2$ ). This underestimated equilibrium saturated concentration was caused by the chosen linear regression, in which, for the largest  $\Delta G$ , the fitted equivalent  $O_2$  concentrations using the linear calibration method were lower than the real equivalent  $O_2$  concentrations (see Fig. 2 (a)).

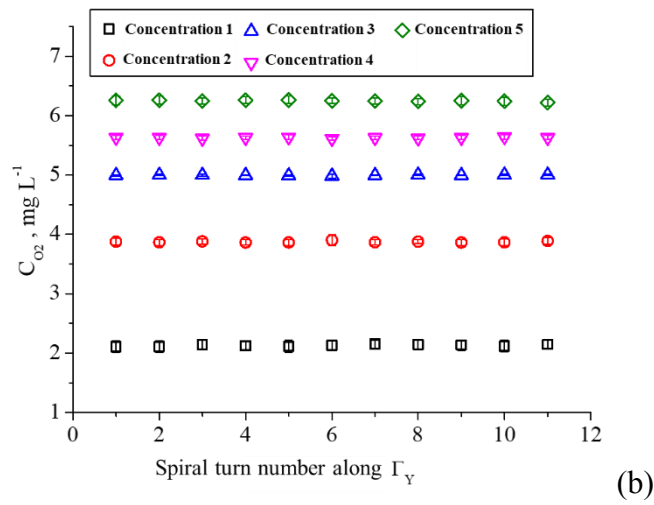
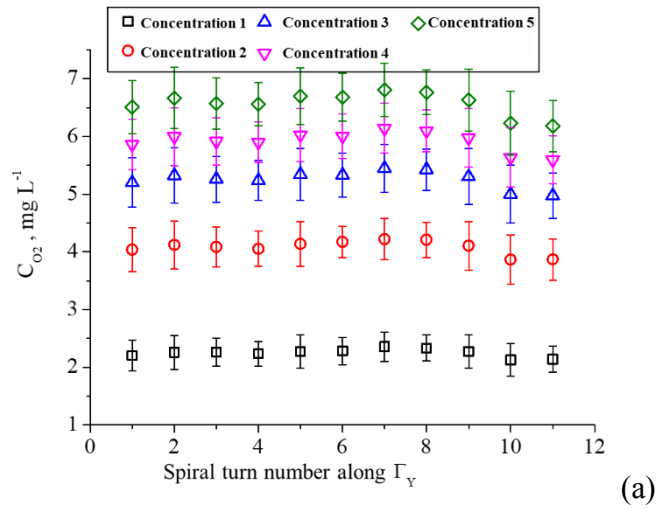


Fig. S1. Profiles of equivalent O<sub>2</sub> concentration along the  $\Gamma_Y$  line at 5 groups of RZ concentrations (numbered from 1 to 5, relating to 0.021, 0.042, 0.0763, 0.084 and 0.105 g L<sup>-1</sup> of RZ, which correspond, based on the reaction stoichiometry, to 1.47, 2.93, 4.40, 5.86 and 7.33 mg L<sup>-1</sup> of O<sub>2</sub>) obtained using (a) the global calibration method and (b) the pixel-by-pixel calibration method.

### 3. Mass transfer interfacial area and Saturated oxygen concentration

The classical Unit Cell model was adopted in the present study, based on the following assumptions:

- The Taylor bubble and liquid slug shape are cylindrical with flat nose and tail (as shown by [Mei et al. \(2020\)](#));
- The liquid slug volume is constant along the channel (as shown by [Mei et al. \(2020\)](#)), and oxygen concentration inside a liquid slug is homogeneous;
- The process is isothermal, so the liquid phase physical characteristics are considered constant and the gas phase follows the ideal gas law;
- The reaction between DH and O<sub>2</sub> is fast and the O<sub>2</sub> transferred into liquid slug is consumed immediately. This means the O<sub>2</sub> concentration in the liquid slug is zero as long as there is still DH in the liquid slug.

The initial O<sub>2</sub> concentration in the gas bubble is  $C_{O_2G}(0) = \frac{p_B(0)M_{O_2}}{RT}$ , where  $p_B(0)$  is the bubble pressure at the bubble formation point, which can be estimated by the initial bubble volume using ideal gas law;

Inside one Unit Cell, the total specific interfacial area consists of two terms:

$$a(X) = a_{LF}(X) + a_{BC}(X), \quad (SI.4)$$

where the specific interfacial area of liquid film and bubble caps, noted  $a_{LF}$  and  $a_{BC}$ , are respectively calculated from:

$$\langle a_{LF}(X) \rangle = \frac{4\langle L_B(X) \rangle}{d_{it}\langle L_{UC}(X) \rangle}, \quad (SI.5)$$

$$\langle a_{BC}(X) \rangle = \frac{2}{\langle L_{UC}(X) \rangle}, \quad (SI.6)$$

where  $\langle L_B(X) \rangle$  and  $\langle L_{UC}(X) \rangle$  are the average bubble and unit cell length, and  $d_{it}$  is the inner diameter of the FEP tube.

As shown in Fig. S2, with increasing  $\eta$ ,  $\langle a_{LF} \rangle$  gradually increased and tended to a constant value, while  $\langle a_{BC} \rangle$  first increased and then decreased gradually. In addition,  $a_{LF}$  could reach 2 to 20 times  $\langle a_{BC} \rangle$ , because the liquid slugs or bubbles were extremely long. This big difference of  $\langle a_{LF} \rangle$  and  $\langle a_{BC} \rangle$  may have resulted in a higher contribution of the lateral bubble body (i.e.,  $k_L \square a_{LF}$ ) than the bubble caps (i.e.,  $k_L \square a_{BC}$ ) to the overall volumetric mass transfer coefficients  $k_L \square a$ .

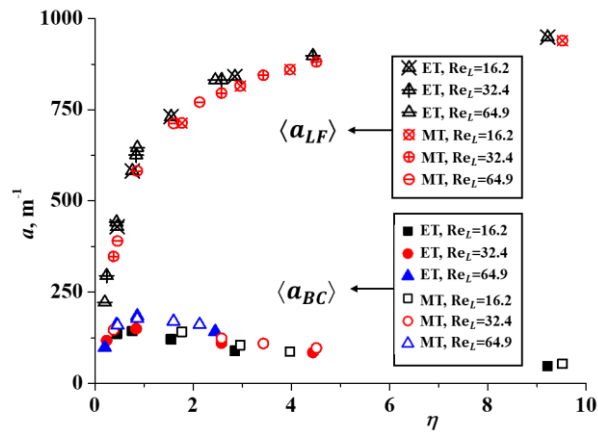


**Fig. S2.** Comparison of the specific interfacial areas  $a_{LF}$  and  $a_{BC}$  for all conditions with increasing  $\eta$ .

#### 4. Saturated oxygen concentration

All along the axial location  $X$ , the  $O_2$  concentration at saturation,  $C_{O_2L}^*$  ( $\text{mg m}^{-3}$ ), will decrease due to the pressure drop and the decrease of  $O_2$  mole fraction in the bubble. Therefore, the driving force ( $C_{O_2L}^* - C$ ) controlling the mass flux inside one Unit Cell will also change.

The variation of  $C_{O_2L}^*(X)$  ( $\text{kg.m}^{-3}$ ) can be described as below:

$$C_{O_2L}^* = H_{O_2}^{cp} \times p_{O_2} \times M_{O_2}, \quad (\text{SI.7})$$

where  $H_{O_2}^{cp}$  ( $\text{mol m}^{-3} \text{ Pa}^{-1}$ ),  $p_{O_2}$  (Pa) and  $M_{O_2}$  ( $\text{kg mol}^{-1}$ ) are Henry's solubility constant, partial pressure of  $O_2$  in the gas phase and  $O_2$  molar mass, respectively.

The dependence of  $H_{O_2}^{cp}$  on the temperature could be neglected because all the experiments were implemented under room temperature,  $H_{O_2}^{cp}$  thus equals to  $1.21 \text{ mol m}^{-3} \text{ Pa}^{-1}$  (Sander, 2015). The partial pressure of  $O_2$  is not only dependent on the bubble pressure,  $p_B$ , but also on the  $O_2$  mole fraction,  $\alpha_{O_2}$ . One could write the mass flux density first from the Taylor bubble gas side (Equation SI.8) and from the liquid bulk side (Equation SI.9), as following:

$$\varphi_{O_2}(X) = \frac{1}{S_B(X)} \frac{-dm_{O_2G}(X)}{dt} = \frac{1}{S_B(X)} \frac{-d(C_{O_2G}(X) \times V_B(X))}{dt}, \quad (\text{SI.8})$$

where  $V_B(X)$  ( $\text{m}^3$ ) and  $S_B(X)$  ( $\text{m}^2$ ) are the bubble volume and bubble interface area, respectively, and  $m_{O_2G}(X)$  (kg) and  $C_{O_2G}(X)$  ( $\text{kg m}^{-3}$ ) are mass amount and mass concentration of  $O_2$  in the gas phase.

$$\varphi_{O_2}(X) = \frac{V_S}{S_B(X)} \frac{d\overline{C_{O_2L}(X)}}{dt}, \quad (\text{SI.9})$$

where  $V_S$  ( $\text{m}^3$ ) is the liquid slug volume.

By combining Equations (SI.8) and (SI.9), the  $O_2$  concentration in the gas phase could be represented as following:

$$C_{O_2G}(X) = \frac{1}{V_B(X)} (V_B^{X=0} C_{O_2G}^{X=0} - V_S \overline{C_{O_2L}(X)}), \quad (\text{SI.10})$$

where the first term on the right is the initial  $O_2$  concentration in the bubble and the second term is the decreasing  $O_2$  amount. The initial  $O_2$  amount can be deduced from the initial bubble pressure, according to:

$$V_B^{X=0} C_{O_2G}^{X=0} = n_{O_2G}^{X=0} \times M_{O_2} = \frac{\alpha_{O_2}^{X=0} \times p_B^{X=0} \times V_B \times M_{O_2}}{RT}, \quad (\text{SI.11})$$

where  $\alpha_{O_2}^{X=0}$  is the initial  $O_2$  mole fraction and equals to 0.21 and  $p_B^{X=0}$  is the initial bubble pressure, which could be obtained by ideal gas law (see (Mei et al., 2020)). For the decreasing  $O_2$  amount, i.e.,  $V_S \overline{C_{O_2L}(X)}$ , the maximum value is achieved when the equivalent  $O_2$  concentration in liquid slug gets saturated, which equals to  $V_S C_{O_2L}^*$ .

To conclude, the maximum percentage of consumed decreasing amount of  $O_2$  to the initial  $O_2$

mole mass is calculated as following:

$$\psi = \frac{V_S C_{O_2Lmax}^*}{V_B^{X=0} C_{O_2G}^{X=0}}, \quad (SI.12)$$

where the maximum saturated O<sub>2</sub> concentration is assumed to be proportional to bubble pressure, hence  $C_{O_2Lmax}^* = \frac{p_B^{t=0}}{P_{atm}} C_{O_2Latm}^*$ ; and the O<sub>2</sub> concentration at saturation (at the atmospheric pressure and 293.15K),  $C_{O_2Latm}^*$ , is found at 8.15 mg/L ([Dietrich et al., 2013](#)). By equation (SI.12), the maximum percentage could be calculated for all the operating conditions, and were found smaller than 10%. These findings show that, in this study, the decrease of O<sub>2</sub> molar fraction  $\alpha_{O_2}$  can be neglected, and thus the saturated O<sub>2</sub> concentration is only proportional to the bubble pressure  $p_B(X)$ :

$$C_{O_2L}^* = H_{O_2}^{cp} \times \alpha_{O_2}^{X=0} \times M_{O_2} \times p_B(X). \quad (SI.13)$$

Because the evolution of  $p_B(X)$  has already been obtained and followed a linear decreasing relation ([Mei et al., 2020](#)),  $C_{O_2L}^*$  decreased linearly along the axial position.

## 5. Calculation of the axial mass flux density and Sherwood number

The procedure implemented to calculate the axial evolution of the mass flux density and Sherwood number is shown in Table S3.

Table S3. Calculation of the axial mass flux density and Sherwood number considering LF (Liquid Film) or not.

<b>Step 1:</b> obtain the oxygen mass $m_{O_2}(X)$ in one liquid slug, kg	
$m_{O_2}(X) = \iiint C(x, y) \cdot dx \cdot dy \cdot dz$	
<b>Step 2:</b> compute the instantaneous mass flux density in one Unit Cell, $\text{kg m}^{-2} \text{s}^{-1}$	
$\varphi_{O_2}(X) = \frac{U_B(X)}{S_B(X)} \frac{dm_{O_2}(X)}{dX}; \text{ combining Eq. (SI. 1) and (SI. 2)}$	
without considering LF	considering LF
$S_B = \frac{\pi d_{it}^2}{2}$	$S_B = \frac{\pi d_{it}^2}{2} \left(1 + \frac{L_B(X)}{2}\right)$
<b>Step 3:</b> calculate Sh number by accumulated mass flux density in one Unit Cell;	
$\text{Sh}(X) = \frac{\langle \varphi_{O_2}(X) \rangle \cdot d_B(X)}{E \cdot C_{O_{2L}}^*(X) \cdot D_{O_2}}; \langle \varphi_{O_2}(X) \rangle_j = \frac{\sum_{i=1}^j [\varphi_{O_2}(X)]_i}{j}, j \leq n; \text{ combining Eq. (SI. 3) and (SI. 13)}$	
without considering LF	considering LF
$d_B = \frac{d_{it}}{\sqrt{2}}$	$d_B = \sqrt{\frac{d_{it}}{2} (d_{it} + 2L_B(X))}$

## REFERENCES

- Dietrich, N., Loubière, K., Jimenez, M., Hébrard, G., Gourdon, C., 2013. A new direct technique for visualizing and measuring gas–liquid mass transfer around bubbles moving in a straight millimetric square channel. *Chemical Engineering Science* 100, 172-182. <https://doi.org/10.1016/j.ces.2013.03.041>
- Mei, M., Felis, F., Dietrich, N., Hébrard, G., Loubière, L., 2020. Hydrodynamics of gas-liquid slug flows in a long in-plane spiral-shaped milli-reactor. *Theoretical Foundations of Chemical Engineering* 54, 25-47. <https://doi.org/10.1134/S0040579520010169>
- Sander, R., 2015. Compilation of Henry’s law constants (version 4.0) for water as solvent. *Atmos. Chem. Phys* 15, 4399-4981.